manuscript accepted for publication in *Geochemistry, Geophysics, Geosystems*

Petrological Evolution and Mass Redistribution in Basaltic Fault Zones: An Example from the Faroe Islands, North Atlantic Igneous Province

Bob Bamberg[1], Marc K. Reichow[1], Richard J. Walker[2], Audrey Ougier-Simonin[3]

[1]School of Geography, Geology and the Environment, University of Leicester, University Road, Leicester LE1 7RH, UK

[2]Department of Earth and Planetary Sciences, University of California, Davis, 1 Shields Avenue, Davis, California 95616, USA

[3]Rock Mechanics and Physics Laboratory, British Geological Survey, Nicker Hill, Keyworth, Nottingham NG21 5GG, UK

Corresponding Author: Bob Bamberg (bobbamberg@gmail.com)

Key Points

- Basalt-hosted fault petrology records progressive stages of fluid-rock alteration followed by dissolution-precipitation cycles of cements
- The main mobile elements are Ca, Si, Al, and CO_2, which are largely reprecipitated as Ca-zeolites and calcite within the fault zone
- Alternating calcite–zeolite mineralisation highlights carbonate activity and metal cation availability feedback during fluid-rock reaction

This manuscript has been peer-reviewed and accepted for publication in **Geochemistry, Geophysics, Geosystems**, but does not include final copyediting and formatting changes. Once the published version is available, it can be accessed via a link on the article webpage.

Abstract

Fault rock petrology exerts an important control on the permeability structure and mechanical properties of fault zones. Slip-related deformation on upper-crustal faults in basaltic rocks is closely associated with fluid-rock interaction, altering the distribution of physical properties within the fault. Here we present quantitative descriptions of the geochemical and petrological evolution of basalt-derived fault rocks, from three passively exhumed fault zones in the Faroe Islands. Fault-rock petrology is determined by optical petrography and automated phase identification based on micrometer-scale chemical maps from scanning electron microscope X-ray spectroscopy. Geochemical evolution is assessed from major and trace element composition measured by X-ray fluorescence. The fault rocks show intense fluid-mediated alteration from a tholeiitic basalt protolith in the damage zones, and mechanical mixing in the fault cores. Pervasive alteration occurs early during fault zone evolution, with incipient fault damage increasing permeability, and allowing along-fault percolation of carbonated meteoric water, increasing fluid-rock ratios. Our results suggest the only mobile species within the fault zones are Ca, Si, Al, which are leached during hydrolysis of volcanic glass and plagioclase, and CO_2, which is added by percolating waters. These species are transported from the damage zones into the fault cores, where they precipitate as zeolite and calcite cements in veins and hydrothermal breccias. We propose that solutes are replenished by cement dissolution through pressure-solution during cataclastic creep, during repeated cycles of hydrofracture and cementation. The fault zones are natural reactors for fluid-mediated alteration by CO_2 and water, while other species are redistributed within the fault zones.

1 Introduction

Basalt is the most common volcanic rock type on Earth (Winter, 2001), and holds great potential to reduce CO_2 concentration in our atmosphere. Basalts can act as a major carbon sink through metal carbonation (Matter et al., 2016; Snæbjörnsdóttir et al., 2020; Lewis et al., 2021) or through intercrystalline adsorption (Stillings et al., 2023). Additionally, the commonly elevated geothermal gradients in basalt formations can be tapped to provide sustainable geothermal energy (Marieni et al., 2018). Faults constitute an important heterogeneity in basaltic sequences, and their stability and permeability are strongly controlled by fault-internal petrological evolution (Walker et al., 2013b; Frolova et al., 2014). Basalt alteration through reaction with residual fluids is thought to start immediately after emplacement during the cooling process (e.g., Mattioli et al., 2016). Alteration commonly takes the form of partial plagioclase replacement (Schenato et al., 2003) and dissolution of volcanic glass and primary minerals, especially olivine, and precipitation of various clay and zeolite minerals, and sometimes calcite, in vesicles (Kristmannsdóttir, 1979; Triana et al., 2012; Mattioli et al., 2016). Early alteration with residual fluids immediately after emplacement is followed by alteration with hydrothermal fluids, and/or meteoric or sea water (Alt and Honnorez, 1984; Schenato et al., 2003; Frolova et al., 2014; Mattioli et al., 2016). Petrological characterizations of fault zones within basalt are scarce but indicate much more extensive alteration than in the surrounding host basalt (Walker et al., 2012; 2013a; 2013b). Such pervasive alteration can have profound implications for fault zone permeability and stability, where interconnected and permeable zeolite veins, and impermeable clay networks may result in a mixed barrier-conduit permeability structure (Walker et al., 2013a; Walker et al., 2013b). In addition, the pervasive replacement of frictionally strong feldspar-dominated assemblages by weaker zeolites

(Yukselen-Aksoy, 2010; Frolova et al., 2014) or clay minerals (Shimamoto and Logan, 1981; Haines et al., 2013; Boulton et al., 2014; Carpenter et al., 2016) can promote mechanical weakening of the fault zone. The structure of the faults analyzed in this study also indicates that fault stability is strongly controlled by fluid pressure evolution and thus permeability structure of the fault (Bamberg et al., 2022).

In this study, we seek to characterize the petrological and geochemical evolution within basalt-hosted fault zones, and integrate these into a conceptual physicochemical model for fault evolution in shallow basalts (Bamberg et al., 2022). Chemical mobility and mass balance within the fault are calculated from X-ray fluorescence whole rock geochemistry. The petrological evolution of the fault zone is reconstructed through optical petrography and high-resolution, automated phase mapping based on X-ray spectrometry in a scanning-electron microscope (a full method is available in the supplement). The results represent a semi-quantitative and qualitative exploration of element mobility and petrological evolution in basalt-hosted faults, rather than a quantitative characterization of chemical fluxes. We sampled three exceptionally well-exposed fault zones in the Faroe Islands Figure 1, that span a displacement range from 30 m to, potentially, kilometer-scale (Bamberg et al., 2022), and cover a full transect of fault rocks, including undeformed protolith, damage zone, fault core, and principal slip zone. Our results indicate that initial pervasive alteration in the damage zone combined with comminution through cataclasis during strain accumulation appear to promote compartmentalization of the fault core, limiting subsequent petrological evolution to zeolite and calcite precipitation and dissolution without communication to external fluid sources.

2 Geology of the Faroe Islands

The Faroe Islands (Figure 1A) are an archipelago located on the European continental shelf of the NE-Atlantic Ocean, between the Shetland Islands and Iceland. Lavas forming the Faroe Islands were emplaced in the Paleogene, during the initial outburst of the Icelandic Plume before the onset of Atlantic rifting, as part of the North Atlantic Large Igneous Province (Ritchie and Hitchen, 1996). Faulting in the Faroe Islands developed during rifting and opening of the NE-Atlantic Ocean. Five overprinting stages of faults and dykes record progressive counterclockwise rotation of the horizontal extension vector, indicating the growth of a continental relay zone between the Aegir and Reykjanes Ridges (Walker et al., 2011; Bubeck et al., 2017). Finally, faults were reactivated as a result of post-breakup passive margin uplift (Gaina et al., 2009; Walker et al., 2011; Gernigon et al., 2012).

The Faroese stratigraphy is dominated by tholeiitic basalts of the Faroe Islands Basalt Group, which are subdivided into seven formations (Passey and Bell, 2007; Passey and Jolley, 2008), with a maximum total stratigraphic thickness of ca. 6.6 km (Figure 1B) (Waagstein et al., 1984; Chalmers and Waagstein, 2006; Passey and Bell, 2007). $^{40}Ar/^{39}Ar$ (Hansen et al., 2002; Storey et al., 2007) and K/Ar & $^{40}Ar/^{39}Ar$ (Waagstein et al., 2002) suggest emplacement between 60 Ma and 55 Ma. The Faroes stratigraphy is summarized in Figure 1B and described in detail by Rasmussen and Noe-Nygaard (1970), Waagstein et al. (1984), and Passey and Jolley (2008). The faults described in this study are hosted in the extensive sheet lobes of the 3.3 km thick Beinisvørð Formation (Í Botni fault zone: Figure 1B & D), the compound lavas of the <1.4 km thick Malinstindur Formation (Gøtugjógv and Selatrað fault zone: Figure 1B & C), and the simple lavas of the 900 m thick Enni Formation (Selatrað fault zone: Figure 1B & C). The younger basalts of the Malinstindur and Enni

126 Formations (Figure 1B) have been subdivided geochemically into two main groups:
127 MORB-derived, low-Ti lavas (TiO_2 < 1.95 wt.%) depleted of incompatible elements, and
128 plume-derived, high-Ti lavas (TiO_2 > 1.95 wt.%) with enriched incompatible element
129 abundances (Gariépy et al., 1983; Hald and Waagstein, 1991; Holm et al., 2001; Søager
130 and Holm, 2009). Both types are dominated by plagioclase-phyric basalts, but low-Ti
131 basalts have on average 4 % higher MgO and a small proportion are olivine-phyric basalts
132 or picrites (Hald and Waagstein, 1991; Holm et al., 2001). A few less-common basalts have
133 also been described, with either intermediate Ti concentrations, high Ti and high Mg
134 (>10 %), or contaminated with lower crustal material (Holm et al., 2001). The Malinstindur
135 Formation, hosting the Gøtugjógv fault zone and parts of the Selatrað fault zones, is
136 dominantly composed of plagioclase-phyric high-Ti basalts (Holm et al., 2001; Søager and
137 Holm, 2009). In the north of the archipelago, the Enni Formation, which is also cut by the
138 Selatrað fault zone, is dominated by phyric and aphyric low-Ti basalts in the lower parts,
139 and both aphyric high-Ti and low-Ti basalts in its upper part.

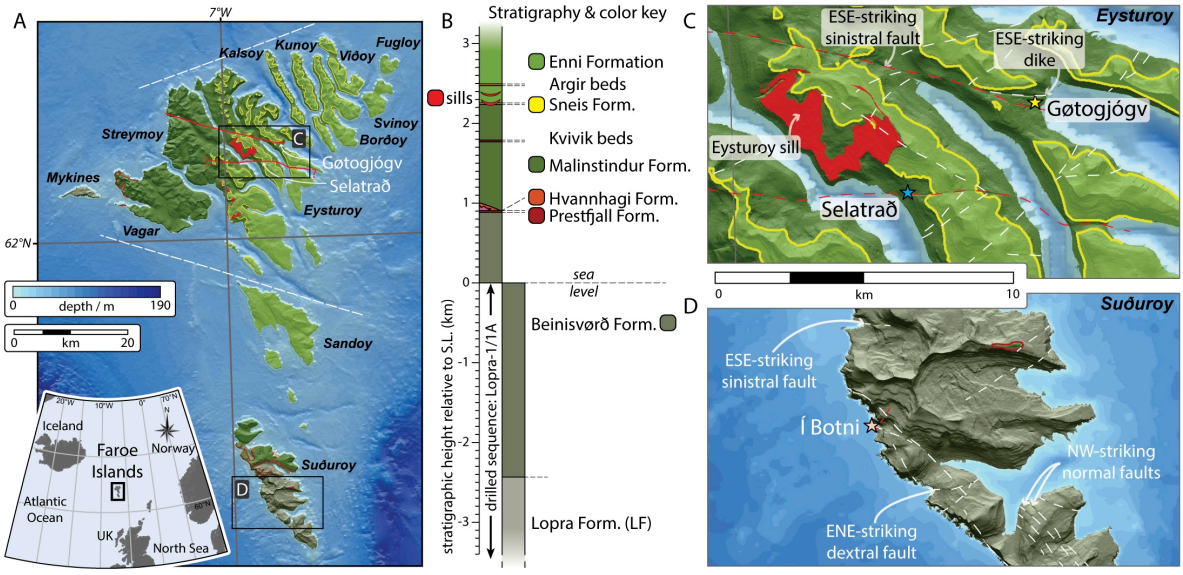

140

141 Figure 1. (A) Geological map of the Faroe Islands. White, dashed lines indicate the
142 proposed locations of large displacement ENE-WSW (unnamed north coast fault; Walker

et al., 2011), and ESE-WNW (Passey, 2009) faults that bound the Northern Islands. (B) Vertical stratigraphic section through the Faroe Island Basalt Group (from Passey and Bell, 2007). Close-up maps highlight the local topography and geology of the (C) Gotugjogv, Selatrad, and (D) I Botni fault zones. See key in B. Studied fault zones are traced in red, other lineaments in white.

3 Structural Framework

The three fault zones analyzed in the Faroe Islands comprise up to decameter-wide damage zones, surrounding meter-wide fault cores that contain multiple cataclastic shear bands and lenticular breccia pods, organized around a central principal slip zone. Fault architecture is described in detail in Bamberg et al. (2022), including fault and fracture distribution, geometry, and deformation mechanisms. Hence, we summarize those aspects here before focusing on the petrological evolution below. The damage zone of the small-displacement fault zone in Í Botni (IBO: location in Figure 1D, detail in Figure 2) consists of a range of variably altered cataclastic breccias (Figure 2B) in contact with the fault core, grading back to undeformed host rock through a zone of chaotic, mosaic, and crackle breccias (fault rock classification from Woodcock and Mort, 2008) (Figure 2B,C). In the large-displacement Gøtugjógv (GOT: location in Figure 1C, detail in Figure 3) and Selatrað (SEL: location in Figure 1C, detail in Figure 4) fault zones, the damage zone is characterized by high concentrations of meter- to decameter-scale fractures and secondary faults. Cataclastic shear bands in the fault core are roughly fault-parallel layers containing altered basalt, fault rock, and/or mineral cement fragments in a heavily comminuted matrix. The most prominent of these shear bands that does not show overprinting by younger structures was identified as the principal slip zone. Shear bands surround lenticular breccia pods of variable clast concentration, that are mineralized with blocky calcite or idiomorphic zeolite (Figure 3B & C). Clasts can preserve the damage zone texture, but show higher degrees of mineral alteration, or more frequently, are fragments of fault rocks and/or mineral cements.

169 These breccia pods become more abundant and extensive with increasing distance from the
170 principal slip zone. Shear bands further away from the principal slip zone tend to be
171 brecciated and mineralized with zeolite and/or calcite (Figure 3E), representing an
172 intermediary state between active shear zone and breccia pod. Moreover, fault cores are cut
173 by fault-parallel, tabular veins of up to decameter apertures and mineralized with the same
174 blocky calcite or idiomorphic zeolite found in breccias.
175 Bamberg et al. (2022) interpreted these structures as evidence for repeated principal slip
176 zone migration and fault core reorganization with intermittent hydrofracture events, where:
177 (1) Permeability reduction in a cataclastic shear band leads to fluid pressurization,
178 triggering hydrofracture and widespread mineralization of the fault core with mechanically
179 strong calcite and zeolite cement; (2) Strengthening forces strain localization into weaker
180 structures of the core, establishing a new principal slip zone; and (3) continued slip leads to
181 older, abandoned structures becoming reworked into the new slip zone.
182

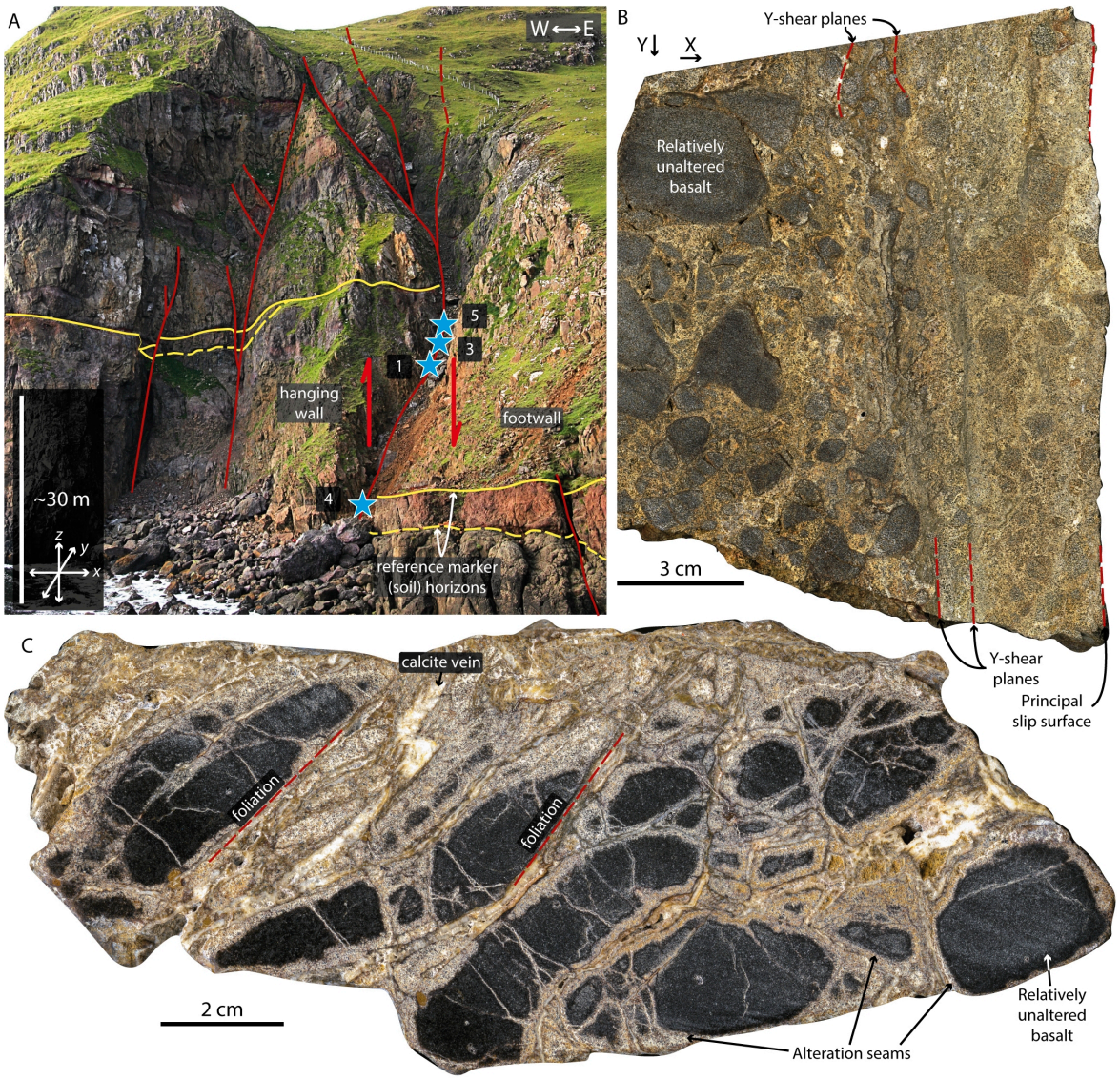

183

184 Figure 2. (A) The I Botni fault zone on Suðuroy is a 50 m wide normal fault with 30 m
185 displacement concentrated on the easternmost strand, as indicated by the marker horizon
186 (yellow). Sample locations are indicated by blue stars. (B: IBO1-3) The fault core (footwall
187 portion preserved on the righthand side of the sample) is bounded by slip surfaces and
188 cataclastic, chaotic breccias coarsening away from the core. (C: IBO1-4) Alteration is
189 limited to the immediate wall rock of fractures and cracks, and rare calcite cements.
190 Localized, black foliation might indicate pressure-solution.
191

4 Results

4.1 Fault Zone Meso- & Microtexture

The unmodified host rock in all localities is a tholeiitic basalt dominated by a plagioclase-pyroxene assemblage including abundant ilmenite and magnetite (Figure 5A & Figure 6A–B). The compound lavas hosting the Gøtugjógv and Selatrað faults can contain <1 cm sized plagioclase phenocrysts, which are absent from the simple lavas in Í Botni. The fine-grained groundmass is composed of opaques (identified as ilmenite and magnetite by SEM-EDS; Figure 6A–B), 50–100 μm glomerates of anhedral pyroxenes, 100–500 μm long euhedral plagioclase crystals, as well as 50–100 μm sized subhedral olivine crystals. The latter have been almost fully replaced by brown, amorphous to fibrous iddingsite ± chlorite (Figure 5A–B). Abundant pockets of brown volcanic glass form an intersertal texture with the plagioclase crystals. The volcanic glass is partially devitrified, often showing radially fibrous rims of a light brown color, enclosing green-brown interior with dark-green interference colors (likely representing palagonite), and sometimes a core of zeolite (Figure 5A–C). Vesicles, most abundant in the porous lava tops, tend to be lined with <50 μm of celadonite ± clay minerals and are filled with coarse zeolite (≤500 μm; Figure 5G & Figure 6C). Optically estimated mineral abundances are: 30 % plagioclase, 35 % pyroxene, 5 % opaques, 10 % olivine and alteration products, and 20 % (devitrified) volcanic glass.

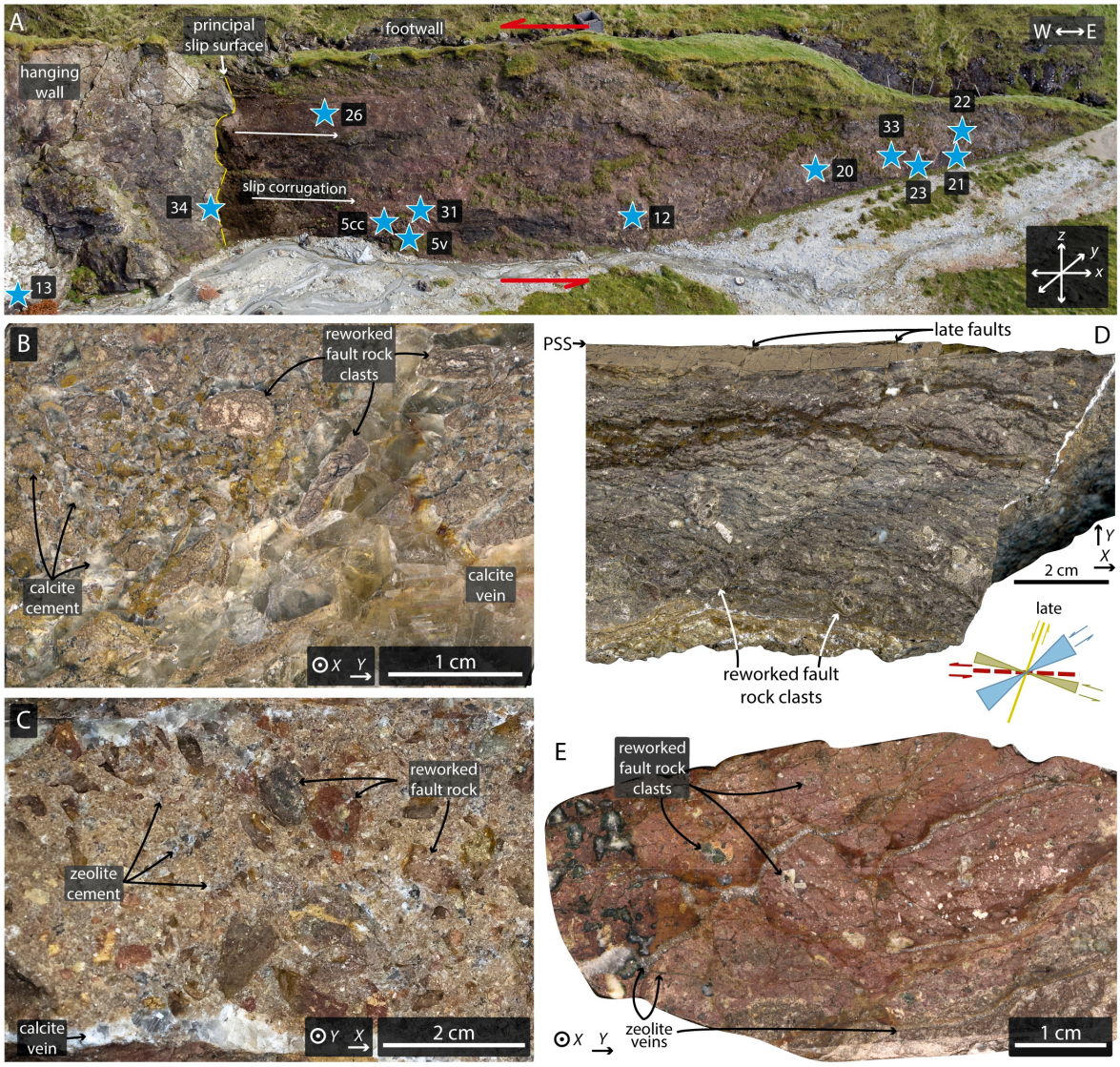

Figure 3. (A) A 50-m-long and 10-m-high diagonal section through the fault core of a sinistral strike-slip fault zone is exposed near Gotugjogv. The corrugated principal slip surface (corrugation plunge shown by arrows) encloses a slip zone of lenticular bodies containing fault rock and bounded by cataclasites. Sample locations are indicated by blue stars. Samples from the fault core also host extensive (B: GOT12) calcite- and (C: GOT5v) zeolite-cemented fault veins that run parallel to the slips surface with angular fault rock fragments. (D: hanging wall slip surface, not analyzed) Cataclasites of the slip surface in some cases are strongly foliated, and show late-stage faults cutting the main foliation. (E: GOT5cc) Cataclastic bands away from the principal slip surface show signs of reworking such as brecciation by zeolite veins. Clasts of reworked fault rock are common throughout the entire fault core.

Within the fault damage zones, plagioclase crystals show an increasing concentration of intracrystalline fractures towards the fault core, which are zeolitised as deep as a few micrometers (Figure 5D). In the vicinity of veins and large-scale fractures, plagioclase breakdown becomes more extensive, with complete replacement in some cases (Figure 5F–G). In early stages of faulting, as shown in Í Botni, the damage zone is brecciated approaching the principal slip zone, grading from mosaic to chaotic breccia at the slip zone contact, with centimeter-scale clasts in a comminuted matrix, and in some places, calcite cement (Figure 2B–C). The ≤50 cm wide slip zone itself is bounded by striated and polished slip surfaces. It is dominated by gouge and cataclasite, with weakly altered host rock clasts (Figure 2B–C), commonly up to a 5 mm in diameter, but sometimes as large as 1–2 cm, in a fine-grained matrix (<25 μm). Clast composition and microtexture is similar to the damage zone rocks described above, with preserved basaltic texture, including fractured and partially zeolitised plagioclase. The matrix is composed of altered host rock that is comminuted to the micrometer scale. Optical discrimination between plagioclase and zeolite in the fine-grained matrix is only possible where plagioclase feldspars display distinctive polysynthetic twinning, inhibiting an accurate estimation of the degree of zeolitisation. However, albite twins can be observed in some matrix grains, indicating that plagioclase zeolitisation is not complete. Further, a brown microcrystalline-amorphous or fibrous phase is common along fractures, resembling iddingsite replacing olivine. The degree of plagioclase zeolitisation can be quantified using SEM-EDS and is described in the next section.

In larger displacement faults (the Gøtugjógv & Selatrað fault zones), small-scale brecciation, as seen in Í Botni, is rare within the damage zone. Instead, the altered host rock

246 described previously is fractured by meter- to decameter-scale secondary faults and smaller
247 fractures, some of which are mineralized with calcite and/or zeolite closer to the fault zone.
248 The fault cores are composed of fault rock lenses bounded by cataclastic shear bands,
249 organized around a prominent slip surface (Figure 3A & Figure 4A). These lenses usually
250 contain cataclasites proximal to the slip surface (Figure 3E), and mineralized breccias
251 closer to the damage zone (Figure 3B–C). The shear bands are composed of ultracataclasite
252 (or gouge), as is a <10 cm thick zone around the slip surface (Figure 3D, Figure 4D,
253 Figure 5I–J). Clasts within the breccia tend to preserve primary basaltic textures, with
254 pyroxene glomerates that show little evidence of alteration despite intense fracturing, and
255 glass in the interstitial space is replaced by opaques, zeolites, and diffuse patches of dark
256 red-brown staining over microcrystalline grains and spherulitic–dendritic opaques
257 (identified as ilmenite by SEM-EDS) (similar to the proximal damage zone; Figure 5C &
258 H). Some clasts are composed of other fault rocks—breccias or cataclasites—and in some
259 cases contain multiple types of fault rock separated by a sharp contact, such as clast-within-
260 clast textures or fragments of wall-rock–vein contacts (Figure 5N–P). These clasts are
261 mostly hosted in well crystallized, millimeter-long bladed zeolite (Figure 5N) and/or
262 <0.5 mm blocky calcite cements (Figure 5O & P). Pore space within zeolite cements is
263 filled with a single crystal (≤1 cm) calcite (Figure 5N). In calcite-cemented breccias, clasts
264 are commonly overgrown with a thin zeolite coating of irregular thickness (<1 mm) (Figure
265 5O), and the cement also contains pockets of zeolite with the contact either following an
266 idiomorphic calcite grain boundary, or showing calcite growth around the zeolite crystals;
267 sometimes both styles are developed in the same pocket (Figure 5P).

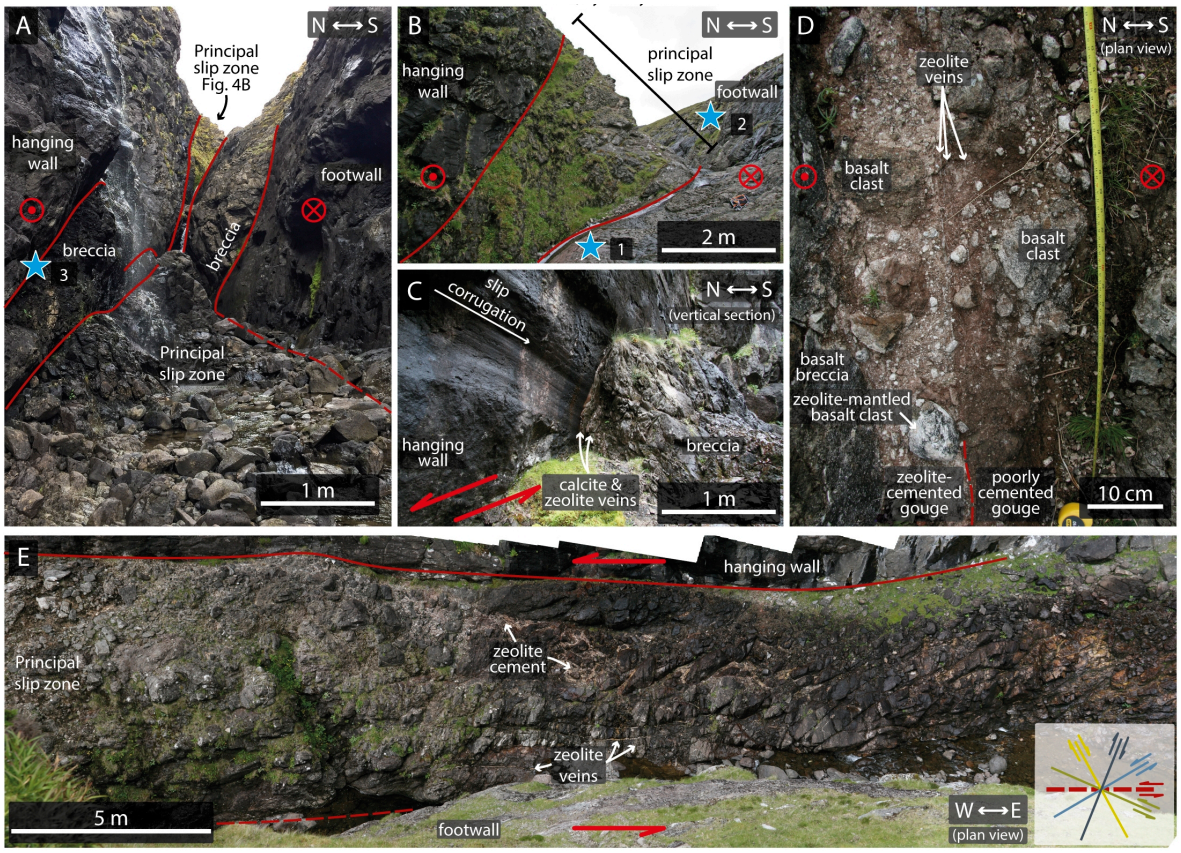

Figure 4. (A) The sinistral strike-slip fault zone at Selatrad is exposed in a deep and long canyon, where a stream has eroded the fault core. Several (A & B) fault rock lenses and (C) polished and striated slip surfaces can be identified. (D & E) The canyon floor shows the fault core with a decameter-thick principal slip surface composed of partially cemented gouge in the north, next to a (E) highly fractured (following Riedel orientations) meter-thick layer in the south.

Many cataclasites in Gøtugjógv and Selatrað are foliated on hand-specimen scale, featuring millimeter-wide, dark red-brown bands parallel to Riedel shear orientations (Figure 3D), and manifesting through a diffuse staining of the matrix on the microscale (Figure 5L). Additionally, some cataclasites show microscopic foliation of aligned, light brown-yellow clay bands separating other grains (Figure 5K). Breccias from Í Botni can contain very narrow black foliae between clasts that resemble pressure-solution seams (Figure 2C & Figure 5E). The cataclasite matrix is commonly stained to a dark red-brown color, and

283 dominated by zeolite and clay minerals, mixed with comminuted pyroxene (<25 μm) and
284 opaques (<10 μm) (Figure 5I). High-magnification SEM-BSE micrographs of the
285 cataclasite matrix show a mixture of angular fragments of zeolite and pyroxene, generally
286 1–5 μm in size, and micrometer- to sub-micrometer-scale, very bright fragments of Fe-
287 and/or Ti-oxides, suspended in a matrix with a platy and/or spongy texture and a grain size
288 ≤2 μm, possibly representing clay minerals (Figure 5J). Many clasts are made up of
289 reworked mineral cements from veins and breccias, sometimes including the contact to the
290 wall rock, but also other cataclasites, or even heavily altered host rock remnants with
291 preserved basaltic texture and amygdales (Figure 5M–P). Ultracataclasites lining prominent
292 slip surfaces are much more homogeneous and have smaller clasts than all other sampled
293 (ultra-) cataclasites (Figure 5I–J). Some cataclasites further away from this slip surface are
294 extensively fractured and brecciated by a network of non-tabular, well mineralized zeolite
295 ± calcite veins (Figure 5M).

296

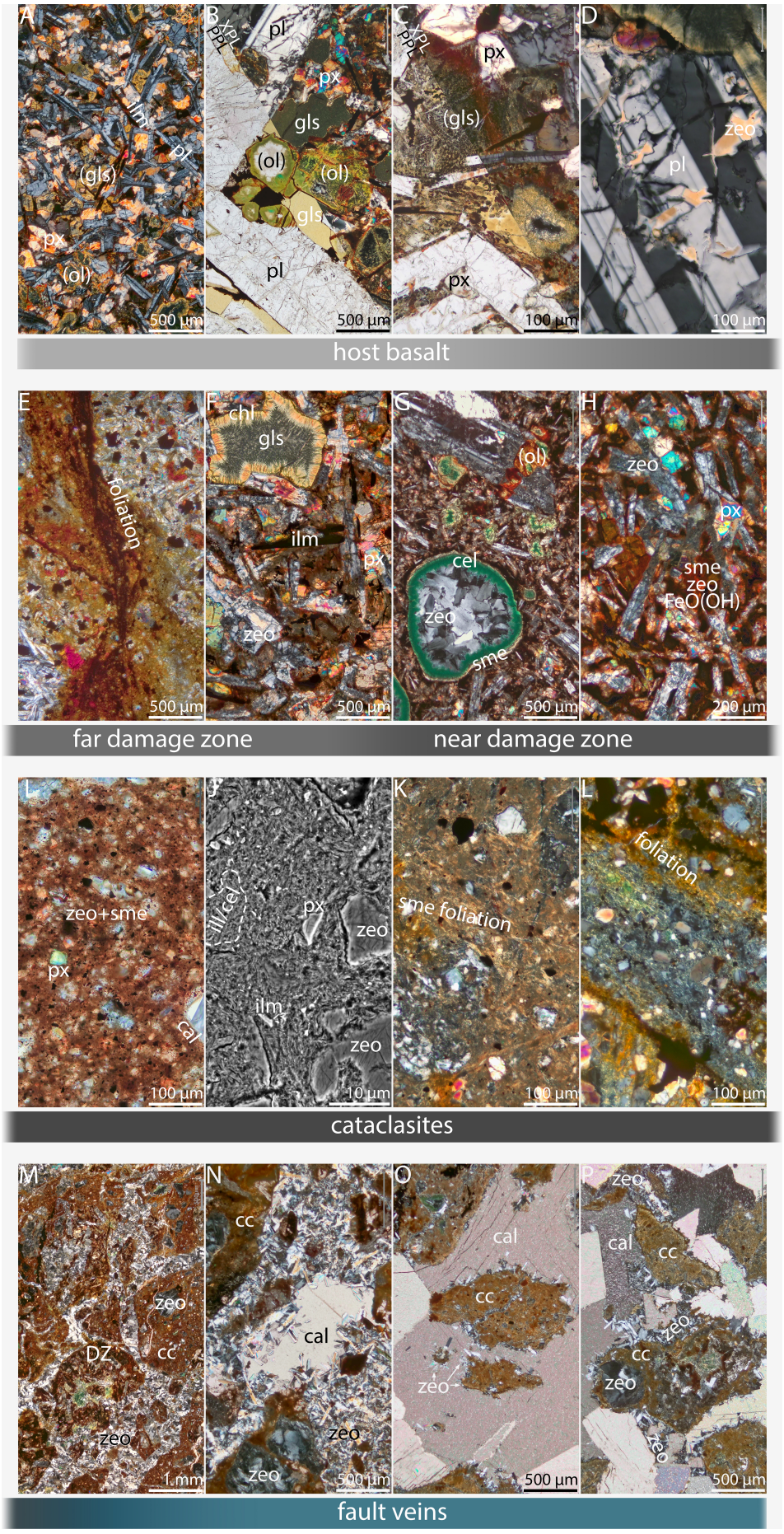
A
ilm
px
(gls)
px
(ol)
500 µm
B
XPL
PPL
pl
px
gls
(ol)
(ol)
gls
pl
500 µm
C
PPL
px
(gls)
px
100 µm
D
zeo
pl
100 µm
host basalt
E
foliation
500 µm
F
chl
gls
ilm
px
zeo
500 µm
G
(ol)
cel
zeo
sme
500 µm
H
zeo
px
sme
zeo
FeO(OH)
200 µm
far damage zone
near damage zone
I
zeo+sme
px
cal
100 µm
J
ill/cel
px
zeo
ilm
zeo
10 µm
K
sme foliation
100 µm
L
foliation
100 µm
cataclasites
M
zeo
DZ
cc
zeo
1 mm
N
cc
cal
zeo
zeo
500 µm
O
cal
cc
zeo
500 µm
P
zeo
cal
cc
zeo
cc
zeo
zeo
500 µm
fault veins

Figure 5. Petrography of basalt-derived fault rocks. (A: GOT13) Tholeiitic host basalt; (B: GOT13) close-up of plagioclase phenocryst with altered volcanic glass and pyroxene in interstitial space (XPL top, PPL bottom); (C: GOT13) secondary minerals derived from volcanic glass breakdown (XPL top, PPL bottom); (D: SEL2) zeolitisation (brown) along intracrystalline cracks in plagioclase; (E: IBO1-4) localized dark foliation in Í Botni damage zone breccia; (F: SEL2) altered basalt in damage zone with prominent, devitrified glass (top right corner); (G: GOT21) celadonite- and heulandite-filled vesicles as well as altered olivine in plagioclase phenocryst; (H: GOT34) close-up of altered basalt with prominent zeolitised plagioclase laths and red stained interstitial space; (I: SEL1) highly comminuted and stained ultracataclastic matrix in slip zone, (J: GOT5cc) SEM-BSE micrograph of cataclastic matrix; (K: GOT26) pervasive, clayey foliation in cataclasite; (L: IBO1-3) some cataclasites show additional, wide foliation defined by diffuse Fe-staining; (M: GOT5cc) brecciated cataclasite with zeolite cement; (N: GOT5v) calcite filling pore in zeolite-cemented fault vein; (O: GOT12) zeolite overgrowth around clast preceding coarse calcite cementation; (P: GOT12) complex intergrowth of zeolite and calcite cements in fault vein. Cal – calcite, cc – cataclasite, cel – celadonite, chl – chlorite, DZ – damage zone, gls – volcanic glass [(gls): altered], ilm – ilmenite, ol – olivine [(ol): altered], pl– plagioclase, px – pyroxene, sme – smectite, zeo – zeolite.

4.2 **SEM-EDS based Mineralogy**

Mineral maps generated from automated phase identification, which were based on element concentrations mapped using EDS, reveal a strong spatial association between plagioclase and zeolite in host and damage zone rocks (Figure 6). Plagioclase grains appear variegated with a network of zeolites and an unclassified mineral phase (Figure 6B–C). Identified zeolites include analcime, most commonly in Gøtugjógv host rock and damage zone, heulandite (more common in the fault core, but also in the Selatrað damage zone sample), or an unspecified zeolite phase which occurs in all samples. Most of this unspecified zeolite phase matches the heulandite classification but with slightly elevated Na and/or reduced Si concentrations. Patches of unclassified material contain individual pixels identified as zeolite, which could indicate that these patches are a zeolitic phase that does not fit into the chemical bounds defined in our recipe (Table S1 in digital supplement). In Í Botni, plagioclase is preserved even in very mature cataclasite next to the slip surface. However, both in Gøtugjógv and Selatrað plagioclase is virtually absent from the fault core

330 (≤ 4 %), while zeolite concentration is markedly increased compared to the damage zone
331 (Figure 6A).
332 Pyroxene concentration remains largely consistent after decreasing by about 10–20 % from
333 host rock to damage zone (Figure 6A). This becomes particularly evident when corrections
334 for varying abundances of vein and amygdale cements are taken into account (i.e.,
335 normalized to the area excluding heulandite, zeolite, and calcite, but including analcime
336 from *in situ* plagioclase replacement). A notable outlier is the cataclasite sample from
337 Selatrað, which has a large area of zeolite-cemented plagioclase fragments and reduced
338 pyroxene concentration. Pyroxenes are disseminated throughout the fault rocks, and
339 decrease in size in more mature rock, while maintaining a high angularity (Figure 5 &
340 Figure 6).
341 SEM-EDS identified most clay minerals in the samples as smectites (i.e., saponite,
342 montmorillonite, or unspecified), illite/celadonite, chlorite, and rare kaolinite (Figure 6).
343 Due to their identical chemical composition, SEM-EDS is unable to distinguish between
344 celadonite and illite, which commonly incorporates Fe and Mg (Deer et al., 2013; Zviagina
345 et al., 2020), hence they are grouped together here. Illite/celadonite is mostly found in the
346 rims of zeolite-filled amygdales in the host rock and damage zone, but also disseminated
347 through fault rocks, though at a very low abundances (Figure 6C–D). The bright green
348 color visible in these zones under an optical microscope indicates that the identified
349 mineral is celadonite rather than illite (Figure 5G). Chlorite concentration is more stable
350 throughout the fault, and it occurs either as an *in situ* alteration product of olivine or glass,
351 or disseminated in the rocks. Glass alteration is most notable in the Selatrað damage zone
352 sample, which contains large (>50 μm) grain-shaped clusters of chlorite, while the most

353 prominent example of olivine can be found in the Gøtugjógv damage zone sample (top left
354 in Figure 6C). This altered olivine grain is composed of a fine-grained mixture of chlorite,
355 illite, and saponite and displays the characteristic intracrystalline cracking of olivine.
356 Measured concentrations of smectites are relatively low in all samples (Figure 6A).
357 Mineral mapping only reveals significant concentrations of saponite in one sample, but, as
358 mentioned above, the texture in high magnification BSE micrographs shows the typical
359 platy and/or spongy texture of clay minerals with grain sizes ≤2 µm (Figure 5J). We
360 discuss the quality of SEM-based mineral mapping in the digital supplement.

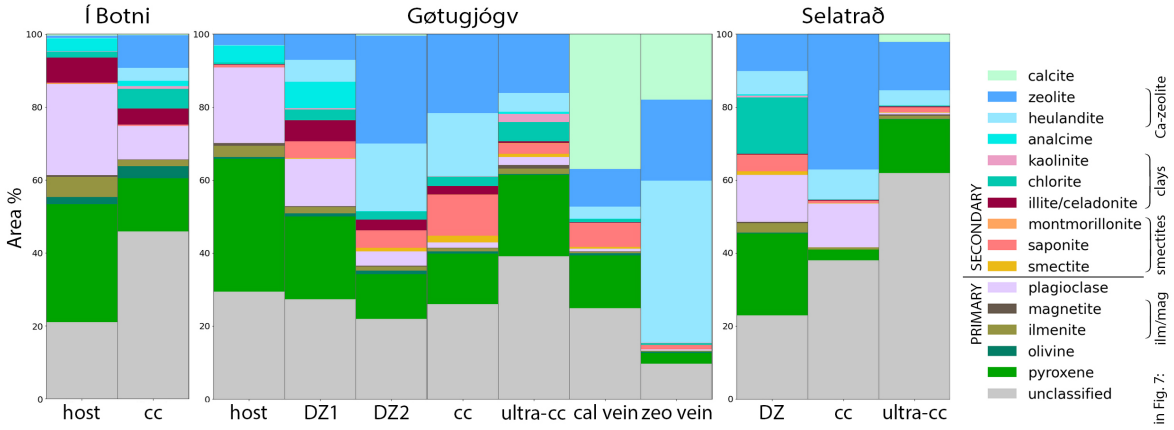

361

362 Figure 6. (A) SEM-EDS mineralogy. Cc – cataclasite, DZ – damage zone, vein – fault vein,
363 zeo – zeolite. IBO host: IBOfwhost, cc: IBO1-3; GOT host: GOT13, DZ1: GOT34, DZ2:
364 GOT21, cc: GOT5cc, ultra-cc: GOT 26, cal vein: GOT12, zeo vein: GOT5v; SEL DZ:
365 SEL3, cc: SEL2, ultra-cc: SEL1.
366

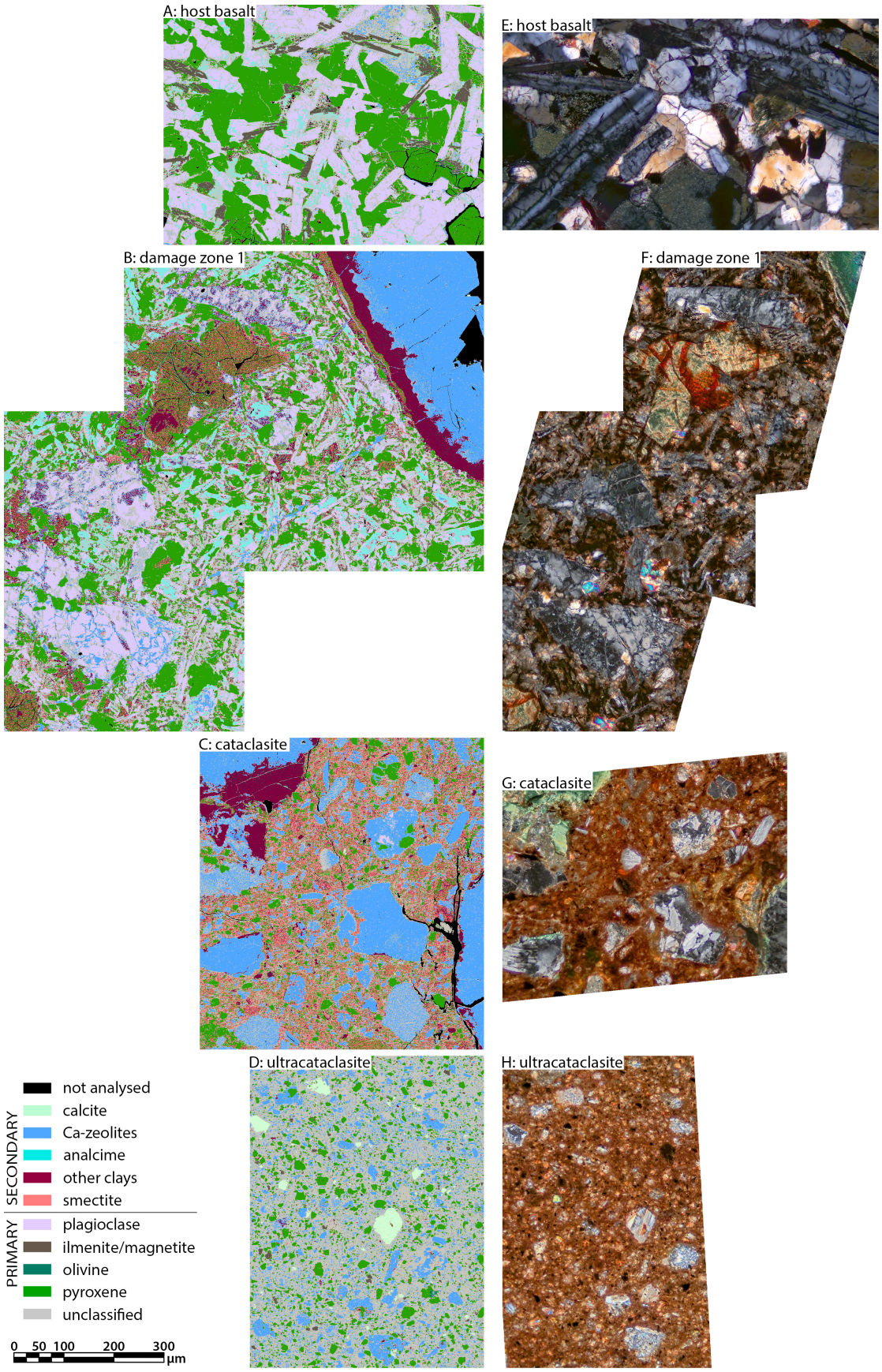
A: host basalt
E: host basalt
B: damage zone 1
F: damage zone 1
C: cataclasite
G: cataclasite
D: ultracataclasite
H: ultracataclasite
not analysed
calcite
Ca-zeolites
analcime
other clays
smectite
SECONDARY
plagioclase
ilmenite/magnetite
olivine
pyroxene
unclassified
PRIMARY
0 50 100 200 300
µm

Figure 7: (A–D) SEM-EDS phase maps and (E–H) corresponding photomicrographs showing the evolution from host basalt to ultracataclasite in Gøtugjógv. (E) is not the exact area mapped in (A) but shows similar texture and mineralogy from the same area of the thin section. (A & E: GOT13) Replacement of plagioclase with analcime in assimilated host rock, (B & F: GOT21) followed by analcime replacement with calcic heulandite, then (C & G: GOT5cc) textural breakdown in cataclasite and complete zeolitisation and argillisation of the cataclastic matrix, and finally (D & H: GOT26) intense comminution in ultracataclasite. The fine grain size of the latter inhibits reliable phase identification. All images share the same scale. Mineral phases have been grouped as indicated in Figure 6. An unsimplified version can be found in the Digital Supplement.

4.3 Fault Rock Geochemistry

4.3.1 Whole Rock Major and Trace Element Composition (XRF)

The plagioclase-pyroxene to zeolite-smectite-pyroxene mineralogy of the samples is reflected in their major element whole rock composition, dominated by SiO_2, Al_2O_3, CaO, Fe_2O_3, and MgO, and minor amounts of Na_2O, K_2O, and TiO_2 (Table 1 & Figure 8). All figures plot anhydrous composition, i.e., re-normalizing major elements to 100 wt.%.

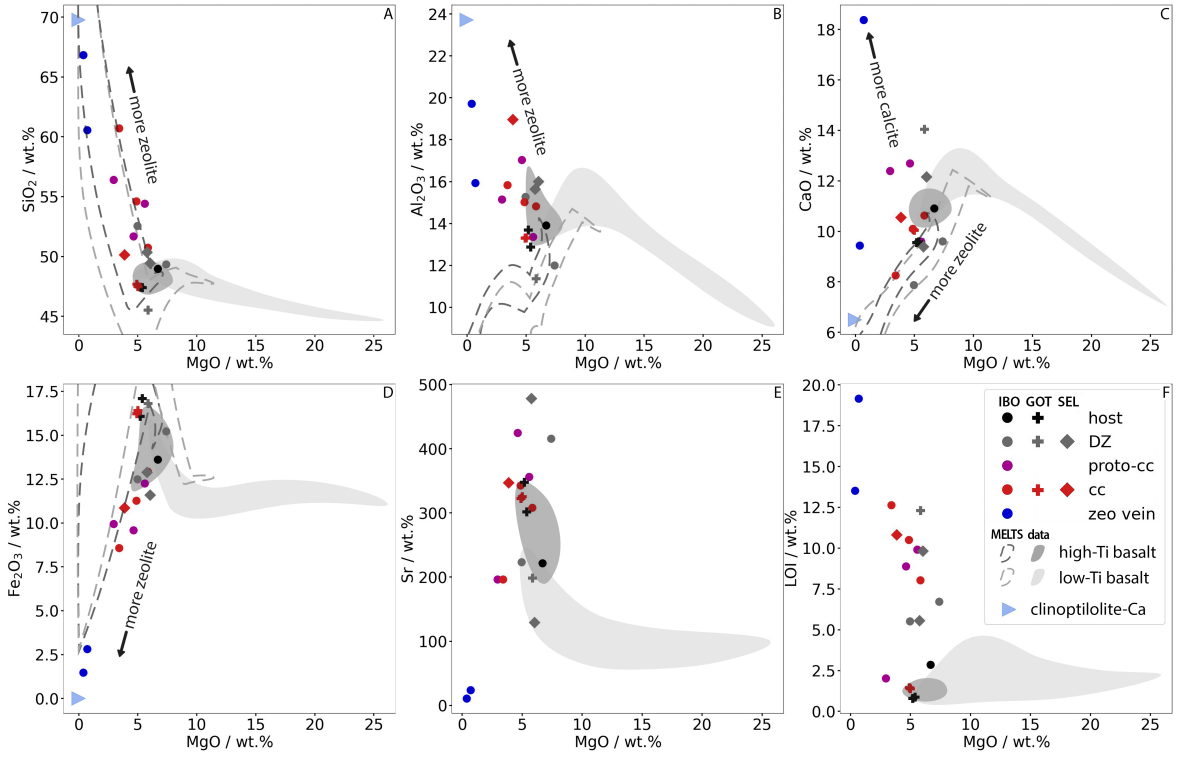

Figure 8. Harker plots showing basalt host and fault rock major and trace element composition. Note, general trend from undeformed high-Ti tholeiitic basalt towards clinoptilolite-Ca composition (blue triangle) in fault veins. The thermodynamic modelling program MELTS (Ghiorso and Sack, 1995; Gualda et al., 2012; Gualda and Ghiorso, 2015), using low- and high-Ti basalt averages as starting composition, was applied to simulate magma evolution through crystal fractionation. The outline of the isobaric calculations spanning temperatures between 1200 and 900°C, at high pressure (1 kbar), low pressure (1 bar) and under three redox conditions (QFM-1, QFM and QFM+1) are indicated by dashed lines. Faroe Island basalt data are taken from Holm et al. (2001) and Søager and Holm (2011). Samples IBO1-1 and GOT12 are not shown because of their high calcite content. Key in F, colors represent different rock types and symbols represent fault zones. DZ – damage zone, cc – cataclasite, IBO – Í Botni, GOT – Gøtugjógv, SEL – Selatrað.

Whole rock chemical composition of our samples falls on a trend from high-Ti basalt composition towards an ideal clinoptilolite-Ca endmember (Figure 8). The protolith and damage zone samples that were the furthest removed from the fault zone, as well as some cataclasite samples coincide with the composition reported for high-Ti basalts in the Faroe Islands (e.g., Holm et al., 2001; Søager and Holm, 2011), while (fault) veins are close to the clinoptilolite-Ca endmember, with compositions of breccias ranging in between. The spread in data observed in our samples is distinct from element distributions observed in Faroe Island basalts and evolutionary trends related to the process of fractional crystallization (e.g., high Al_2O_3 and CaO contents) as illustrated in Figure 8. The chemical composition remains largely unchanged throughout the fault zone (Figure 9), the only major excursions being samples with abundant calcite (IBO1-1 & GOT12) or zeolite cement (GOT23 & GOT5v). Due to the low number of samples from Í Botni and Selatrað, the following description will focus mainly on samples from Gøtugjógv. The patterns described there are reflected in the data from the other two fault zones.

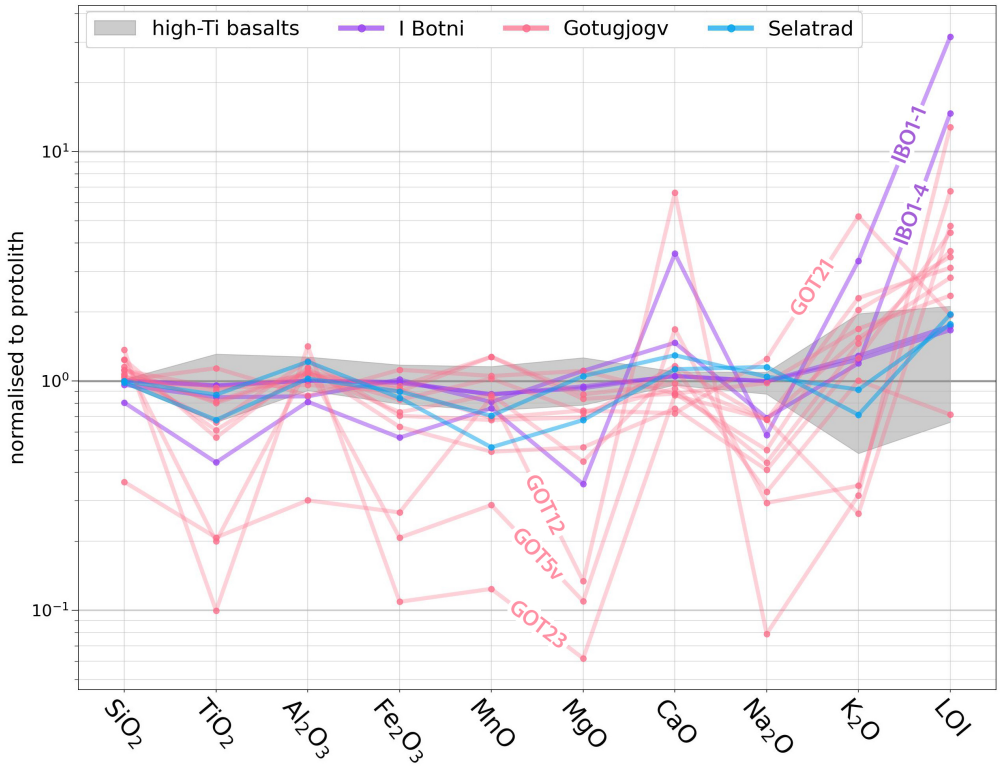

413

414 Figure 9: Composition of fault rock samples normalized to their respective host rock (mean
415 IBO host, GOT13, SEL2) and high-Ti basalts on the Faroe Islands (Holm et al., 2001;
416 Søager and Holm, 2011) normalized to mean composition of the high-Ti basalts. Only
417 zeolite-cemented fault veins (GOT23 and GOT5v) and calcite-cemented fault veins
418 (GOT12 and IBO1-1) show strong deviations.
419
420 The protolith samples selected as a reference for further analysis are the most pristine rocks
421 that were accessible close to the fault outcrops, and fall within the typical basalt
422 composition reported for the Faroe Islands (Figure 10). They are averaged Í Botni hanging
423 wall and footwall host rock (samples IBOhwhost & IBOfwhost), Gøtugjógv hanging wall
424 host rock (GOT13, Figure 5A & C), and the relatively unaltered wall rock from a distal
425 damage zone fracture in Selatrað (SEL2, Figure 5B & D). Petrographic analysis and SEM-
426 EDS mineralogy (Figure 6) of the Í Botni host rock samples show a fully preserved basaltic
427 assemblage with unaltered calcic plagioclase, pyroxene, glass, and opaques, but olivine has
428 been replaced with iddingsite. The Gøtugjógv and Selatrað samples show minor

429 plagioclase alteration along intracrystalline fractures, as well as partial glass breakdown
430 (Figure 5A–D).

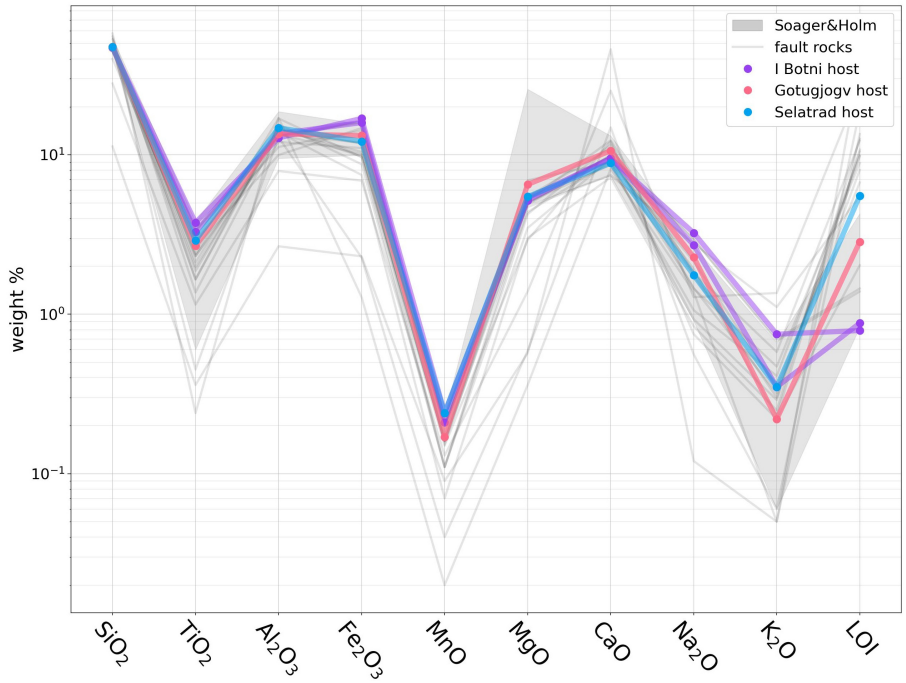

431

432 Figure 10. Major element composition of protolith sample used for each fault zone and
433 published data for different basalts from the Faroe Islands (Søager and Holm, 2011) and
434 fault rock samples. Note that all protoliths plot on the upper end of the TiO_2 range and
435 lower end of the MgO range.
436

437 We assess element mobility in the faults by comparing fault rock composition to the local
438 protolith using isocon diagrams (Figure 11) (Grant, 1986; Ague, 1991; Hippertt, 1998).
439 Figure 7 reveals that Zr, and to a lesser extent TiO_2, MgO, Cu and Zn remain immobile
440 during fault rock deformation. We therefore used Zr in the following as a reference element
441 to calculate global mass change (i.e., how much mass a unit of protolith lost or gained
442 during chemical alteration: Figure 12) and element mobility (Figure 13 & Figure 14).
443 Global mass change (mass of the altered sample M^A versus mass of protolith M^0) can be
444 calculated via the concentration of the immobile element in the altered sample C_i^A

compared to the concentration of the immobile element in the protolith C_i^0 using (Grant, 1986; Ague, 1991):

$$\frac{C_i^0}{C_i^A} = \frac{M^A}{M^0} \quad (1)$$

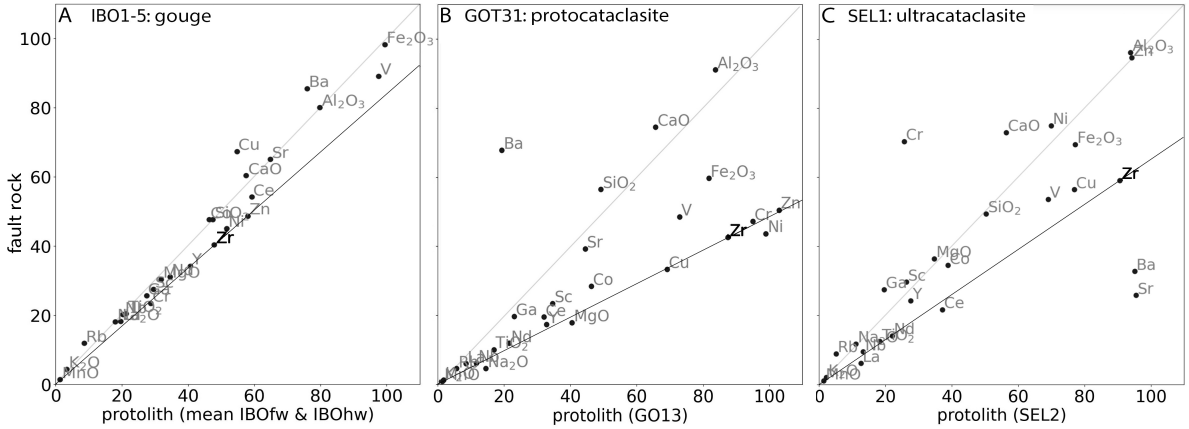

Figure 11. Representative isocon diagrams from each fault zone, plotting fault rock against protolith compositions. The selected protolith samples are the most pristine rock that was accessible at each fault zone. The black isocons connecting immobile elements plot below the light grey constant mass reference line, indicating mass gain in all three samples. Isocon diagrams for all analyzed samples can be found in the digital supplement.

In Gøtugjógv, the relative mass change compared to host rock records a mass loss (-7 %) in the damage zone, 0.5 m away from the fault core (GOT34) compared to protolith, and mass gains (ca. 23 %) in the damage zone directly in contact with the core (GOT21), increasing to up to 105 % in cemented breccias (GOT20), and returning to 23 % in the ultracataclasite sample (GOT26). For the fault veins, total mass gain ranges between 490 % (GOT5v) and 1000 % (GOT23). Selatrað shows a similar pattern with mass gain of 53 % in the ultracataclasite (SEL1), while Í Botni shows a relative mass change within ~20 %, where cement is absent, and up to 200 %, where cemented with calcite (IBO1-1) (Figure 12).

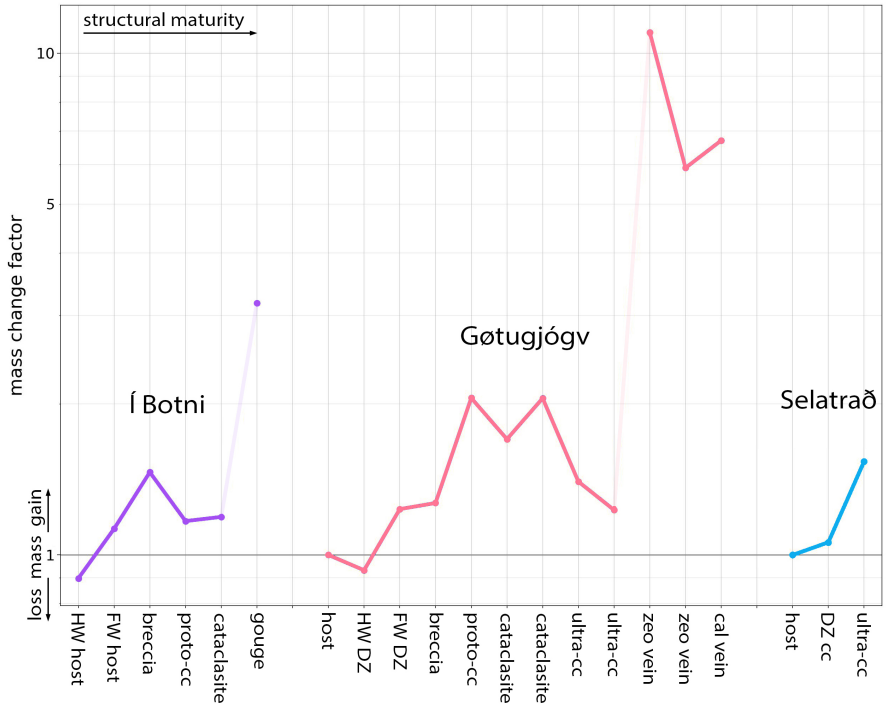

Figure 12. Global mass change compared to local protolith (M^A / M^0, Eq. 1). Protoliths are mean IBO host, GOT13, and SEL2. Values <1 denote mass loss (e.g., leaching), whereas values >1 denote mass gain (e.g., cementation). Sample names in Table 1. Cal – calcite, cc – cataclasite, DZ – damage zone, FW – footwall, HW – hanging wall, zeo – zeolite.

Diagrams of element concentration plotted against immobile Zr for all samples show the mobility of individual oxides/elements undistorted by the effect of global mass change (Figure 13 & Figure 14). Immobile elements plot on the isocon connecting the origin to the protolith. Samples that plot above the isocon have gained the relevant oxide (i.e., they are enriched), whereas samples that plot below the isocon are depleted relative to the host rock. The plots reveal dominantly fault internal redistribution of SiO_2, Al_2O_3, CaO, and LOI. With the exception of the calcite-cemented breccia (not shown in plots), all samples fall on a linear trend intersecting the isocon around the position of host rock composition. The most distal damage zone rocks are relatively depleted of mobile elements, and zeolite veins are strongly enriched; cataclasites and breccias plot in between. K_2O shows increasing

enrichment from veins, to cataclasite and breccia, and further to damage zone samples, relative to host rock, with the most significant enrichment in sample GOT21. K_2O is mainly contained in illite and celadonite, which are associated with amygdale linings and thus the primary porosity of the protolith. The host rock sample derives from a massive lava core with minimal porosity, and consequently low K_2O concentration. All other elements plot along their respective isocon, with normalized concentrations decreasing progressively from the damage zone, through cataclasites and breccias, to veins.

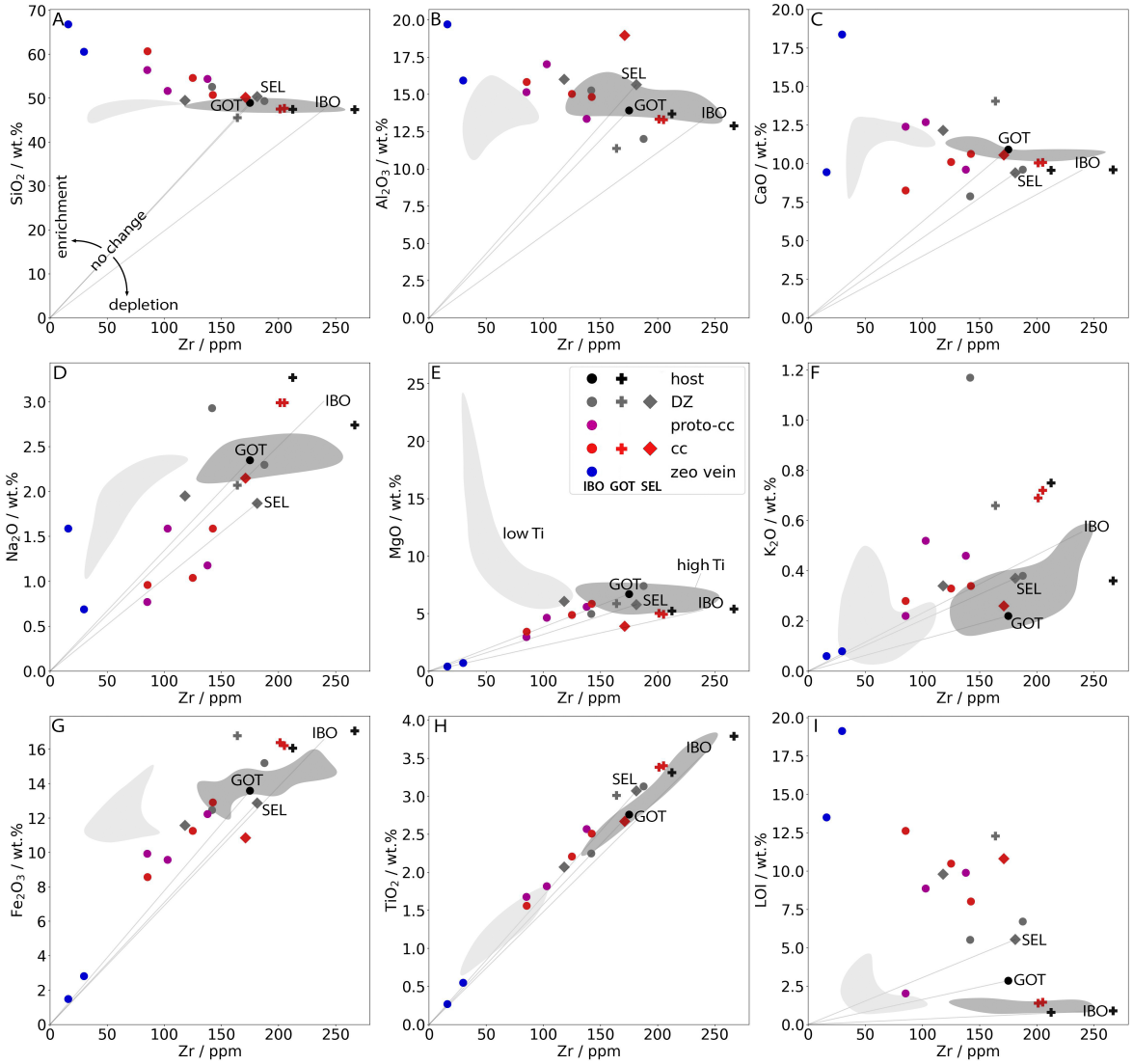

Figure 13. Covariance plots for major elements and immobile Zr visualize element mobility during alteration. The isocon connecting the origin with the protolith approximates the path for isochemical evolution from the protolith, samples plotting below are depleted in the studied element and samples plotting above are enriched. Only Si, Al, and Ca show significant deviations from the isocon, indicating that these elements are mobilized during fault rock alteration. They are depleted in the damage zone and enriched in the fault core and zeolite fault veins. Samples IBO1-1 and GOT12 are not shown on the plots because of their high calcite content. The composition of Faroese basalts taken from Holm et al. (2001) and Søager and Holm (2011) is plotted in light (low-Ti) and dark (high-Ti) gray fields. Key in E, colors represent different rock types and symbols represent fault zones. DZ – damage zone, cc – cataclasite, IBO – Í Botni, GOT – Gøtugjógv, SEL – Selatrað.

Trace element concentrations generally follow the same trend as Zr. The only exceptions are Ba and Sr, as well as in some cases Cr, Sc, V, and Ni (Figure 14). Elevated Ba/Zr ratios indicate Ba enrichment in the Gøtugjógv damage zone, especially in the hanging wall. In the more mineralized samples, such as breccias and veins, the absolute concentrations of Ba and Zr are reduced due to the addition of zeolite/calcite cements, but Ba/Zr ratios stay similar. A similar trend can be observed for Sr in Gøtugjógv. Í Botni fault rocks show only slightly elevated Sr, Sc, and Ni in the calcite cemented fault rock breccia. Similarly, calcite-dominated rocks from Gøtugjógv have high Cr, Sc, and V. In the Selatrað fault rocks, Ba and Sr are slightly depleted, and Cr and Sc are strongly enriched in the ultracataclasite. Ba and Sr (and perhaps Cr) correlate with Fe concentration, while V and Sc correlate with Ca. It should be noted that Ba concentration in the Gøtugjógv host rock is about half the concentration of published Faroe Island basalts data (Søager and Holm, 2011) as well as 1/3–1/5 of the concentrations in Í Botni and Selatrað, respectively.

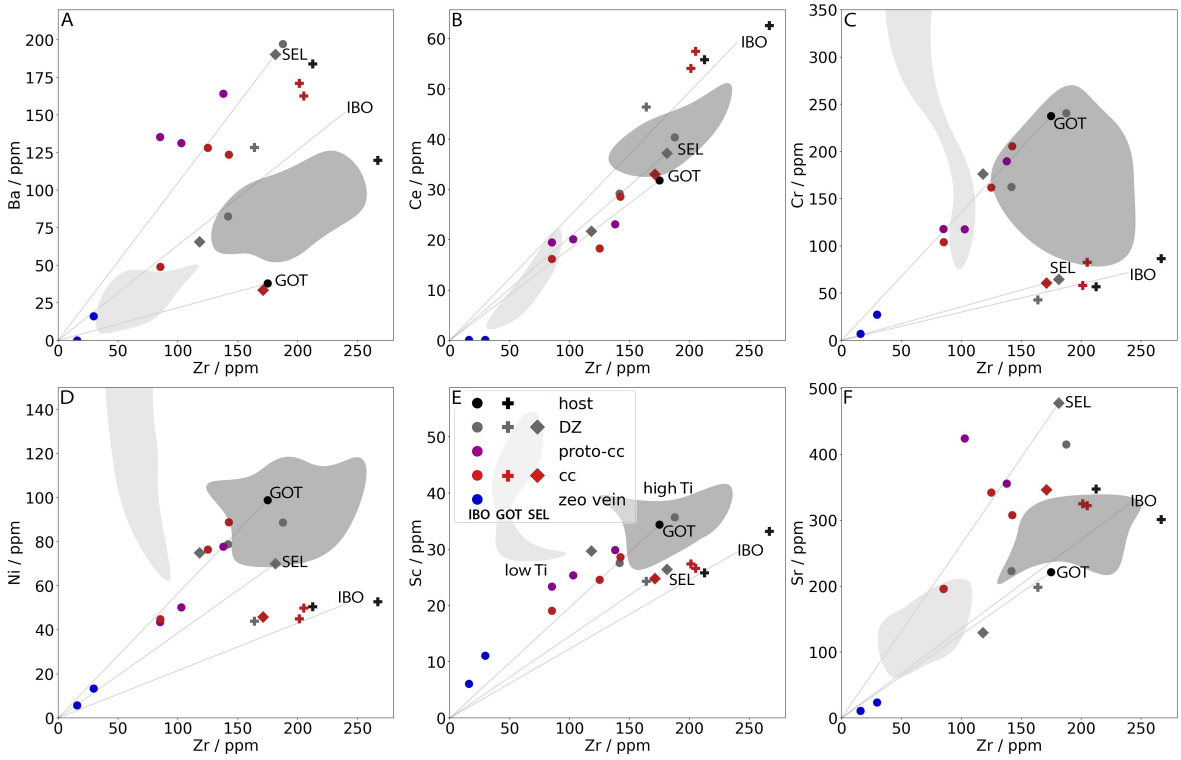

Figure 14. Covariance plots for selected trace elements and immobile Zr. Samples IBO1-1 and GOT12 are not shown on the plots because of their high calcite content. Geochemical data for different basalt types (low-Ti in light and high-Ti in dark gray) are taken from Holm et al. (2001) and Søager and Holm (2011). Key in E, colors represent different rock types and symbols represent fault zones. DZ – damage zone, cc – cataclasite, IBO – Í Botni, GOT – Gøtugjógv, SEL – Selatrað.

4.3.2 **Element Distribution in Minerals (SEM-EDS)**

All samples show almost complete olivine and glass breakdown and replacement by chlorite, mixed smectite, and unidentified phases. These secondary phases have high concentrations of Fe and Mg.

In the damage zone, Na is strongly concentrated in analcime at the expense of plagioclase, which is partially replaced. Ca concentration is not increased in the remnants of plagioclase compared to unaltered plagioclase, however anorthite/albite ratios increase from 1.1 in host rock to ≤3.1 in the fault core, consistent with preferential dissolution of albite. Only about

529 30–40 % of plagioclase is replaced by analcime. Besides plagioclase, Ca is concentrated in
530 heulandite/clinoptilolite (which form a continuous solid solution series and are referred to
531 as Ca-zeolite in the following) and other zeolite phases (excluding analcime), filling
532 vesicles or replacing plagioclase closer to the fault core. Zeolites tend to have a higher Si
533 and a lower Al concentration than plagioclase. The volcanic glass and secondary minerals
534 filling interstitial space in between plagioclase and pyroxene grains (or remnants) have
535 variable compositions, either similar to Fe-Ca-pyroxene or a Na-Ca-zeolite. Mg
536 concentration in pyroxenes remains stable across the entire fault zone. However,
537 Fe/Fe+Mg+Ca in pyroxene decreases by about 10 wt.% from host rock to cataclasite in Í
538 Botni, and then another 10 wt.% to samples from Gøtugjógv and Selatrað, whereas the
539 relative Ca concentration increases by only about 1 wt.%. The only other phases containing
540 Mg are rare saponite and illite/celadonite, the latter also concentrating most of the K.
541 In the fault core, analcime is absent and Na is only abundant in remnant plagioclase. The
542 remaining Na, as well as K, is contained in very low concentrations in zeolites and
543 unidentified phases of the cataclasite matrix. Ca concentration is more homogeneous across
544 the fault core compared to the damage zone or host rock, as it is relatively evenly
545 distributed between zeolites, smectites, and unidentified phases, and abundant only in
546 pyroxene and calcite cements. In fault core breccias, Fe is still chiefly contained in
547 pyroxenes and ilmenite/magnetite, but also secondary phases from glass and olivine
548 breakdown. In the cataclasite matrix, Fe concentration is consistently high, exceeding the
549 concentration in pyroxene. Si is abundant in zeolite grains of the (ultra-) cataclasites,
550 whereas Al is more evenly distributed between zeolites, smectites, and unidentified phases.
551 Ultracataclasites from Gøtugjógv and Selatrað, as well as the cataclasites from Í Botni,

have a high concentration of unidentified matrix with no measurable Mg, low Si, but high Al, Ca, and Fe.

5 Interpretation & Discussion

5.1 Mineralogical Composition and Evolution

Examination of undeformed host rocks indicates that the earliest phase of alteration affects olivine and volcanic glass (Figure 5A–C), which is common in a wide range of alteration conditions (Gislason and Eugster, 1987a; Frolova et al., 2014; Mattioli et al., 2016). Unaltered olivine is rare in the samples, including the protolith (Figure 5A), indicating that its breakdown is diagenetic rather than related to faulting. Olivine replacement minerals are classified as a mixture of saponite and chlorite (Figure 6C), and 'pyroxene' which more likely represents a mixed phase analysis (i.e., a mixel) or secondary Fe-Mg silicate (with minor Ca but no Al). Common alteration products of olivine are iddingsite and clay minerals, such as celadonite and nontronite (Alt and Honnorez, 1984; Mattioli et al., 2016). Volcanic glass and its alteration products are commonly classified as chlorite but show a distinct Mg gain, and Si (+Al) loss in fibrous alteration rims compared to the massive cores. Optically, the fibrous rims closely resemble palagonite (Figure 5F), even though the chemical composition does not match such a mixed smectite-zeolite phase. Volcanic glass is at least partially devitrified before deformation-related alteration, based on the zeolitic cores observed in protolith samples. Fibrous rims (Figure 5A) might be chlorite, as suggested by SEM-EDS mineralogy, whereas the green-brown cores are probably another cryptocrystalline Fe-Mg silicate with lower Fe and Mg, and higher Si content than the surrounding chlorite. Volcanic glass is often found to be replaced by aggregates of cryptocrystalline zeolites (Frolova et al., 2014), clays and Fe-oxy-hydroxides (Alt and

Honnorez, 1984; Mattioli et al., 2016) or a mixture of those (Ghiara et al., 1993). Unclassified secondary phases resulting from *in situ* glass devitrification are most likely smectites, zeolites, and Fe-oxy-hydroxides (Hawkins, 1981; Gislason and Eugster, 1987a; Mattioli et al., 2016). The latter are visible in thin sections as opaques (Figure 5C) and might cause the observed brown-red coloration (Figure 5E–I); the small grain size of these phases inhibits phase identification using SEM-EDS.

Fault rocks representative of early damage are associated with a reduction in relative Fe concentration in pyroxenes (e.g., Í Botni), crossing from pigeonite to augite composition. This released Fe may contribute to red staining within the damage zone and cataclasites (Figure 5E–I), which we suggest primarily binds onto clay minerals. This is followed by *in situ* plagioclase zeolitisation, first into analcime (incorporating only Na, and releasing Ca) and then also other, more calcic (7–10 wt.% Ca, 1–3 wt.% Na) zeolites around fractures and veins, where more abundant fluids promote element mobility (Figure 5D–H, Figure 6B–C). Alteration to analcime only affects about 30–40 % of plagioclase (Figure 6A–C), possibly limited by the availability of Na.

Fault core rocks, representing initial deformation localization, indicate that analcime and the remaining plagioclase are replaced by more calcic zeolites (Figure 6B–C). Similarly, coarse, idiomorphic zeolites (dominantly Ca-zeolite) fill vesicles (Figure 5G & Figure 6C). Stable Na concentrations (Figure 13D) imply that secondary zeolitisation scavenges Na locally, probably at the expense of plagioclase and older zeolites. Na concentration should be increased in samples with abundant zeolite if significant amounts were transported by the pore fluid, as is the case for Ca (Figure 13C).

Composition of the brown-red, fine-grained matrix in (ultra-) cataclasites is more puzzling. Large areas could not be identified from their EDS spectra (Figure 6E), and the grain size is too small for identification by optical petrography (Figure 5I–K). The platy to spongy habit observed in SEM-BSE micrographs (Figure 5J) suggests abundant clay minerals (Frolova et al., 2014; Mattioli et al., 2016), mixed with equant zeolite and pyroxene fragments. However, the matrix contains no Mg (average composition: 5 wt.% Fe, 12 wt.% Al, 22 wt.% Si, 10 wt.% Ca, ≤2 wt.% Na), which cannot be reconciled with the mineral composition suggested above. Assuming the measured Fe represents small amounts of magnetite or Fe-oxy-hydroxide mixed with the main constituent phase, the remaining chemistry roughly matches a non-specific zeolite composition (with, in atoms per formula unit, 23 O, 13 Al, 7.3 Ca, and 1.9 Na, assuming 72 O in the oxide formula). In this case, the platy/spongy textures observed in SEM-BSE might have resulted from dissolution reactions. Gislason and Eugster (1987a, their Figure 1B) observed similar reaction textures in their dissolution experiments of crystalline basalts, although at 10× larger scales.

5.2 **Pore Fluids**

The fault rocks described in this study show evidence of fluid-mediated alteration focused around sites of elevated permeability such as veins and fractures. Groundwater chemistry data is not available for the Faroe Islands (Eidesgaard et al., 2019). The present-day hydrologic system may be similar to that of Iceland or East Greenland, which have a similar geology and geography. In both regions, low-temperature geothermal springs (<150 °C) are fed by meteoric water that is thought to form convection zones in fracture and fissure swarms (Arnórsson, 1995b; Hjartarson and Armannsson, 2010). Icelandic low-temperature waters (Table 2) are generally neutral to slightly alkaline (pH 6.1–10.6) and

carbonated (<4100 ppm, but generally between 15–60 ppm CO_2), with similar concentration ranges for SiO_2 (Gislason and Eugster, 1987b; Arnórsson, 1995b). Cation concentrations are low (<20 ppm) except for Na, which typically reaches hundreds-of-ppm (Arnórsson and Barnes, 1983; Gislason and Eugster, 1987b; Arnórsson, 1995b; Aggarwal et al., 2000).. High-temperature geothermal fluids (Table 2) have a similar cation concentrations, but are slightly acidic and reducing, with H_2S generally ranging in the tens- to hundreds-of-ppm (Gislason and Eugster, 1987b; Arnórsson, 1995a).

At the time of faulting, the Faroe Islands experienced a much hotter climate as they were emplaced during the Paleocene-Eocene Thermal Maximum, with global temperatures 5–8 °C higher than present-day (McInerney and Wing, 2011). Groundwater chemistry in the young Faroe Islands might therefore be more similar to present day Hawaii or the Deccan Traps. Groundwater samples collected in a borehole on the summit of Kilauea (Table 2) are slightly alkaline (pH ~8) and have higher cation concentrations than Icelandic geothermal waters and similar concentration ranges for SiO_2 and carbonate (reported in HCO_3) (Tilling and Jones, 1991; Hurwitz et al., 2003). They are thought to form through mixing of meteoric groundwater and magmatic gas (Hurwitz et al., 2003). At the coast, groundwater composition (Table 2) only marginally deviates from seawater, with enrichment limited to SiO_2 (Thomas et al., 1996). In the Deccan Traps, groundwaters (Table 2) have a similar acidity and HCO_3 concentration, while cation concentrations tend to be on the lower end of the concentration spectrum from Kilauea (Kale et al., 2021). We observe strong enrichment of Ba and Sr in the Faroese damage zones, compared to the protolith (Figure 14A & F). This suggests that pore fluids might be of meteoric origin and percolated down through the highly fractured damage zone. Ba and Sr would be mobilized during plagioclase and matrix

643 breakdown and transported along the fault during downward flow in the damage zone, until
644 they are incorporated into secondary phases such as clays and Fe-oxy-hydroxides (Das and
645 Krishnaswami, 2006). Ba has been found to accumulate in the matrix and, to a smaller
646 degree, in plagioclase phenocrysts (Philpotts and Schnetzler, 1970; Bindeman and Davis,
647 2000). Sr is thought to dissolve from primary basalt phases, especially feldspar and
648 volcanic glass at shallow depth, and then accumulate in zeolites of the heulandite-stilbite
649 zone, resulting in a vertical gradient (Neuhoff et al., 2000). Since Ba and Sr are precipitated
650 in the damage zone, they are depleted in cements of the fault core precipitating later-on.
651 Alternative fluid sources would be seawater, or upwelling geothermal fluids. Our data do
652 not show increasing Na-concentrations in altered rocks, which could be expected if they
653 were reacting with fluids similar to the seawater-derived groundwaters in Hawaii (Thomas
654 et al., 1996). Hot geothermal fluids in Iceland are reducing due to high H_2S concentrations
655 (Arnórsson, 1995a). However, virtually no SO_3 is found in our samples (Table 1), and red
656 staining indicates oxidizing conditions in the fault zone. Major element concentration in the
657 fault zone only deviates significantly from host basalt in zones that contain abundant
658 mineral cements (Figure 9 & Figure 13). Even there, only CaO, SiO_2, and Al_2O_3 are
659 enriched, and LOI is similarly elevated. Element mobility diagrams (Figure 13 & Figure
660 14) show that fault rocks consistently plot between two endmember compositions: altered
661 damage zone (e.g., GOT34) and pure zeolite (± calcite) vein (e.g., GOT23), showing that
662 cementation is the only notable chemical influence after initial host rock alteration. Mineral
663 cements are dominantly calcite and Ca-zeolite (Figure 5N–P & Figure 6A), hinting at the
664 presence of a carbonated fluid. As fault rocks from the low-displacement fault in Í Botni
665 only contain calcite cements (Figure 6A), and calcite is also the dominant cement in the

fault-distal damage zone in Gøtugjógv and Selatrað, we infer that the pore fluid initially contains relatively high carbonate concentrations. Carbonated, low-temperature groundwaters are common in Iceland (Arnórsson and Barnes, 1983; Gislason and Eugster, 1987b; Arnórsson, 1995b; Aggarwal et al., 2000), which has a similar geological setting to the Faroe Islands. Zeolite precipitation would only be possible after significant dissolution of Si and Al during damage zone alteration. A likely source for these elements is volcanic glass, where we can observe a distinct Si and Al loss from the potentially unaltered cores to the fibrous secondary minerals in the rims. This is supported by studies indicating order-of-magnitude higher dissolution rates for basaltic glass compared to crystalline basalt or its mineral components (e.g., Gislason and Eugster, 1987a), and the onset of volcanic glass dissolution is accelerated in carbonated, alkaline fluids (Hawkins, 1981), like those found in Iceland. As Ca does not accumulate in remnant plagioclase during replacement with analcime, which only incorporates Na, it must be released into the fluid. The same reaction also produces Si and Al as by-products. Basaltic glass dissolution has also been proposed as a source for Ca, Al, and Si, triggering zeolite mineralization in oceanic basalts (Alt and Honnorez, 1984; D'Antonio and Kristensen, 2005) as well as altered basalts in Scotland (Triana et al., 2012).

As indicated by the element mobility diagrams (Figure 13), CaO, Si_2O, and Al_2O_3 are transported from the damage zone to the fault core, where they are sequestered in zeolite and calcite cements. The lack of evidence for any external chemical input other than CO_2 and water suggests that the fault core may trap fluids. This is also supported by permeability measurements on basalt-derived fault rocks from the Faroe Islands, which show a high potential for cross-fault sealing with low permeability zones between the host

689 rock and damage zone, and again between damage zone and fault core (Walker et al.,
690 2013a; 2013b). This sets the faults on the Faroe Islands apart from the more widely studied
691 upper-crustal suboceanic faults with strong hydrothermal overprinting (Agar, 1990;
692 Hayman and Karson, 2007, 2009), or faults in deep sheeted dyke complexes (Varga et al.,
693 1992), or (serpentinized) suboceanic gabbro (Boschi et al., 2006; Zihlmann et al., 2018),
694 which all record hydrothermal overprinting and significant deviation from the protolith
695 composition. Leaching of a large volume of damage zone rocks should release enough Ca,
696 Si, and Al for the spatially limited cementation of the fault core (explored further in the
697 next section). Alternation between zeolite and calcite precipitation is probably linked to
698 evolving carbonate activity in the fluid (Zen, 1961; Neuhoff et al., 2000). Early calcite
699 precipitation in Í Botni and replacement of plagioclase with Na-zeolite (i.e., analcime) in
700 Gøtugjógv indicate an initially high carbonate activity, preventing the precipitation of
701 Ca-zeolites (Zen, 1961; Neuhoff et al., 2000). Parts of the damage zone that are assimilated
702 into the fault core become hydraulically isolated by the surrounding, impermeable
703 cataclasites, limiting fluid exchange and pressure equilibration. Carbonate activity would
704 be reduced progressively as plagioclase and volcanic glass alteration releases Ca, Si, and
705 Al into the fluid, and calcite is precipitated. As a result, conditions would become more
706 favorable for Ca-zeolite precipitation. However, as zeolite cementation removes significant
707 amounts of Ca, Si, and Al from the fluid, especially following hydrofracture, carbonate
708 activity would rise again, and the remaining porosity is filled with calcite. Ca-zeolites are
709 the dominant precipitate as long as its components are sufficiently concentrated in the fluid,
710 but through their depletion carbonate activity increases and eventually prevents further
711 zeolite precipitation. Zeolite precipitation tends to remove silica faster from the solution

712 than it is being released from volcanic glass (Hawkins, 1981). At this stage, calcite is
713 deposited until one of its building blocks is exhausted, leaving a pore fluid that is depleted
714 in all mobile species.
715 As we see evidence for repeated alternation between calcite and zeolite cementation in the
716 fault cores (Figure 5N–P), a mechanism controlling the phase that is precipitated is needed,
717 as well as one that allows for replenishment of the solutes (i.e., Ca, Al, Si, CO_2) following
718 a hydrofracture and cementation event. The transition from zeolite to calcite precipitation is
719 probably controlled by increasing carbonate activity in the evolving fluid (Zen, 1961;
720 Neuhoff et al., 2000), as outlined above. A potential mechanism for replenishing solutes is
721 partial reassimilation of zeolites and calcite (and potentially other mineral phases) through
722 pressure-solution during and/or following cataclastic creep. The thick layers of cataclasites
723 around slip surfaces suggest that most displacement in the fault core is accommodated by
724 cataclastic creep, which is often accompanied by pressure-solution (e.g., Hadizadeh, 1994;
725 Gratier et al., 2014) of mobile phases such as calcite and zeolites. Several samples, such as
726 Í Botni breccias and some cataclasite from Gøtugjógv and Selatrað show discontinuous and
727 curved foliae defined by accumulation of clays and opaques and could be interpreted as
728 pressure-solution seams (Figure 5E & L). High mobility of the otherwise immobile Al in
729 the fault zones seems surprising at first, but can be explained in the light of the petrological
730 evolution of the fault rocks. Initial mobilization occurs during metasomatic replacement of
731 plagioclase with much less stable analcime and Ca-zeolite. These zeolites could then be
732 repeatedly dissolved through pressure-solution and reprecipitated during episodic
733 hydrofracture. Various degrees of zeolite dissolution in creeping cataclasites could
734 potentially also explain the variable concentration of residual clays in the matrix of (ultra-)

735 cataclasites. However, these compositional inconsistencies could also have arisen from
736 local variability in protolith composition (e.g., fault veins yielding more zeolite, and
737 assimilated damage zone rocks yielding more clay). Processes for fluid replenishment that
738 lack a mechanism for cement dissolution, such as fluid influx from an external source,
739 would lead to a progressive dilatation of the fault core and the increasing dilution of
740 residual basalt alteration products by Ca, Si, and Al, at increasing displacements, which is
741 not supported by our data (Figure 12, Figure 13, Figure 14).
742 Finally, the lacking evidence for fluid replenishment in the fault cores implies that failures
743 or potential ruptures of the fault zone are limited to the fault core, and do not typically
744 breach the core–damage zone boundary, as this would result in fluid ingress from the
745 permeable damage zone. Hence, mature faults in basalts should present a relatively stable,
746 hydrologically closed system and act as quasi-permanent barriers to cross-fault fluid flow.
747 Such a permeability structure is corroborated by permeability measurements of Faroese
748 fault rocks (Walker et al., 2013a; Walker et al., 2013b).

749 ### 5.3 **Mass Balance**

750 If a fault core remains hydrologically sealed during its evolution, the gross budget of
751 solutes has to balance out across the sealed fluid cell in the fault zone. The mass change
752 factors of individual elements T_m, as plotted in the element mobility graphs (Figure 13),
753 can be used to calculate the volume of leached damage zone material necessary to balance
754 enrichment in the fault core.

755 $$T_m = \left(\frac{C_i^0}{C_i^A}\frac{C_j^A}{C_j^0}\right) - 1 \qquad (2)$$

Where C_i is the concentration of the immobile element and C_j is the concentration of the mobile element in the altered fault rock (C^0) and protolith (C^A) (Grant, 1986; Ague, 1991). Since we cannot appreciate the lateral extent of fluid cells from our data, we can only calculate a balance across a one-dimensional section of the fault zone, in which we use the thickness of each sampled subzone instead of volume. This way, we can estimate the necessary thickness of leached rock by comparing the sum of the mass change factor in each subzone weighted by the subzone's width (W_{zone}) from all subzones that gained the considered species (i.e., positive mass change factor), to all the subzones that lost the species (i.e., negative mass change factor).

$$\sum_{enriched} T_{m,zone} \times W_{zone} \; + \sum_{leached} T_{m,zone} \times W_{zone} \; = 0 \qquad (3)$$

In the Gøtugjógv fault zone, this suggests that SiO_2 mobilization in ca. 12 m of damage zone is required to balance the enrichment through zeolite mineralization in the core and near damage zone (Table 3). Similar calculations suggest that about 4 m and 11 m of damage zone could provide the Al_2O_3 and CaO required to balance their enrichment in the fault core (see digital supplement for calculation). The true thickness for CaO is likely to be lower, as we have included a relatively pure, 5 cm wide calcite vein in our calculations to provide an upper bound, but calcite veins in the fault zones usually contain significant amounts of zeolite and clasts (Figure 3C), which reduces their Ca concentration. It should also be noted that the thicknesses we calculated are very rough estimates, since we assumed a homogeneous mass change factor for each subzone, but their heterogeneity is likely to resemble the microtextural complexity of fault rocks. Nevertheless, leaching of a 4–12 m wide damage zone is possible in Gøtugjógv, where the total width of the damage zone is around 13 m.

5.4 **Depth of Faulting**

Amygdales in the analyzed fault rocks are almost exclusively filled by a thin lining of celadonite and less abundant smectites, followed by coarse heulandite/clinoptilolite towards the center (Figure 5G & Figure 6C), which is also the most common cement in the fault zone (Figure 6). Heulandite and clinoptilolite have been found to destabilize around the same temperature (ca. 450 °C and 450–550 °C) in laboratory experiments (Ghiara et al., 1999), which might suggest that clinoptilolite in our samples is stable in the same temperature range. This would place the fault zones in the heulandite/stilbite stability zone, from 90–100 °C to 110–130 °C (Kristmannsdóttir and Tomasson, 1978; Jørgensen, 2006). Illitisation of smectite minerals, which is commonly used for temperature estimation (Pytte and Reynolds, 1989; Velde and Vasseur, 1992), is most likely inhibited by the low availability of K in the study area. Using these temperature ranges and geothermal gradients proposed by Jørgensen (2006), ranging from 56 °C/km in the Enni formation to 66 °C/km in the Beinisvørð Formation, combined with estimated timing of faulting (syn-volcanic for Í Botni, post-volcanic for Gøtugjógv and Selatrað; Walker et al., 2011) fault cements and amygdale fills would have precipitated at depths of 1.4–2.0 km in Í Botni and 1.5–2.1 km in Gøtugjógv and Selatrað. This is slightly deeper than expected from zeolite mapping performed by Jørgensen (2006), which would place Í Botni and Gøtugjógv in the shallower mesolite zone between 1.0 km and 1.5 km. Notably, our analysis did not reveal any mesolite in the samples, even though it is compositionally closer to plagioclase than analcime, which forms during the first stage of zeolitisation. Fault-parallel fluid migration could potentially modify the geothermal gradients within fault zones. Upward welling of hot hydrothermal fluids could result in an increased gradient, whereas downward percolation of meteoric water could reduce the gradient. In the case here, the latter is more

803 likely, and could therefore imply that the faults were active at slightly greater depth than
804 suggested above.

805 5.5 Implications for Fault Evolution

806 The studied fault zones cut through plagioclase-pyroxene dominated basalts with minor,
807 diagenetically altered olivine, and partially devitrified volcanic glass (Figure 5A–C, Figure
808 6B). We apply a space for time substitution for fault rock assemblages, to summarize
809 observations into a conceptual fault zone evolution model (Figure 15).
810 In the incipient fault zone (or at the edge of the damage zone), damage accumulation
811 increases permeability and fluid-rock ratios (Bamberg et al., 2022). Meteoric, carbonated,
812 and slightly alkaline water percolates along the damage zone, where it catalyzes early
813 metasomatic alteration. Initially, Na-rich plagioclase is replaced by analcime, and volcanic
814 glass continues to break down into smectites, zeolites, and Fe-oxy-hydroxides (Figure 5C–
815 H, Figure 6B–C). This releases Ca, Al, and Si into the fluid (Figure 13), and leads to
816 chemical weakening of the rocks (Frolova et al., 2014). Carbonate activity is reduced in the
817 evolving fluid through calcite precipitation and mineral dissolution, until Ca-zeolites
818 become the dominant precipitate. The weakened rock localizes deformation into a principal
819 slip zone, establishing a fault core where displacement is accommodated by cataclastic
820 flow (Figure 2B, E–G, Figure 5I, Figure 6D–E). Cataclastic comminution and the potential
821 accumulation of smectites reduce permeability, compartmentalizing the fault zone. Since
822 fluids are now trapped in the core, chemical exchange and pressure equalization with the
823 damage zone are inhibited (Figure 13). Fluids become pressurized due to compaction,
824 eventually triggering hydrofracture (Proctor et al., 2020) and rapid cementation of the fault
825 core (Figure 3B–C, F, Figure 5M–P). Zeolite precipitation depletes dissolved Si, Al, and

826 possibly Ca, increasing carbonate activity in the fluid, and the remaining voids are filled
827 with coarse calcite (Figure 5N–P). Widespread cementation strengthens the core, forcing
828 slip zone migration into a weaker domain (Bamberg et al., 2022). The abandoned slip zone
829 is reworked by cataclasis (Figure 3D–E) (Bamberg et al., 2022) while pressure-solution
830 could dissolve some of the cements and replenish solutes in the fluid. Comminution and
831 cement dissolution reset the stage for a subsequent hydrofracture event, and the fault zone
832 continues to evolve through episodic cycles of cementation-strengthening and shear-
833 compaction (Bamberg et al., 2022) with the only significant mineralogic changes being
834 cement precipitation and dissolution.
835

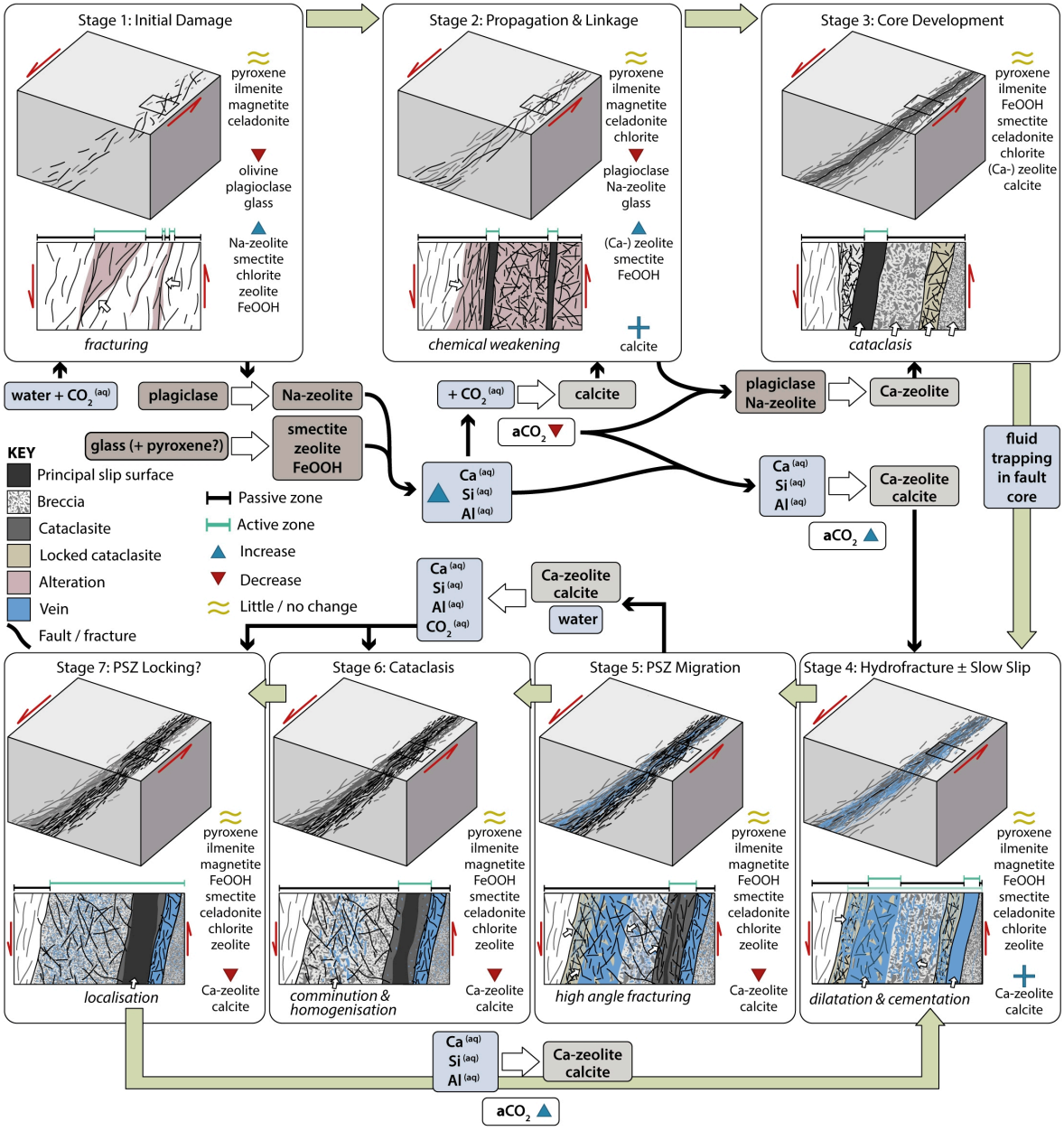

836

837 Figure 15. Conceptual model of fault evolution outlining the relative timing of petrologic
838 alteration building on the structural model from Bamberg et al. (2022). Damage
839 concentration in the early fault or damage zone increases permeability and thus fluid
840 availability (Stage 1). Alteration of primary phases such as volcanic glass and plagioclase
841 with carbonated waters releases Si, Al, and Ca into the fluid (Stage 1–2). As a result,
842 carbonate activity in the evolving fluid drops and the primary precipitates change from
843 analcime (Na-zeolite) and calcite to Ca-zeolites (Stage 2–3). Low-permeability shear bands
844 of comminuted and pervasively altered cataclasites trap fluids in the fault core, isolating the
845 fault-internal fluid system (Stage 3). Ongoing shear increases internal fluid pressure,
846 eventually triggering hydrofracture and rapid cementation with zeolites (Stage 4), which
847 strengthen the core and force slip zone migration (Stage 5). Cataclastic creep in the new

slip zone is accompanied by pressure-solution of calcite and zeolite cements, replenishing solutes in the fluid (Stage 6–7) and setting up the fault for a next pulse of hydrofracture and cementation (Stage 4). aCO_2 – CO_2 activity, (s) – solid, (aq) – aqueous.

6 Conclusions

Basalt-hosted fault zones in the Faroe Islands are sites of intense petrological alteration, featuring almost complete textural and mineralogical breakdown of the tholeiitic protolith. Olivine and volcanic glass alteration starts during diagenesis, but the primary phases are only completely replaced in damage zones breccias, where damage concentration increases fluid-rock ratios. Olivine is replaced by smectite, chlorite, and an unidentified Fe-Mg silicate that can incorporate some Ca. Volcanic glass is replaced by aggregates of zeolite, smectite, and Fe-oxy-hydroxides. In the vicinity of the fault core, zeolites replace plagioclase. Zeolitisation progresses through two stages, where Na-rich plagioclase is replaced by analcime, followed by Ca-zeolites replacing the remaining anorthite-dominated plagioclase and analcime. Only pyroxene and ilmenite/magnetite remain relatively unaltered. In the fault core, secondary phases, pyroxene, and ilmenite/magnetite are mechanically mixed through cataclasis. After incorporation of water and CO_2, chemical mobility is limited to alternating Ca-zeolite and calcite precipitation and dissolution; the latter probably by pressure-solution during cataclastic creep in the core. The only mobile species are Ca, Si, Al, and CO_2. Carbonate is most likely added through meteoric waters percolating through the damage zone, whereas the fault cores appear to be largely hydrologically sealed, inhibiting chemical exchange or fluid-pressure equilibration with the damage zone and host rock.

Acknowledgements

We thank Tom Knott and Leon Hicks for their technical support on the SEM, and Lin Marvin-Dorland for her help during XRF analysis. We also wish to thank Catriona Menzies, David Holwell, Jeremy Rushton, and Zhenchao Zang, as well as the reviewers Nick Hayman and Jessica Warren for their valuable feedback that greatly improved this manuscript.

Data Availability Statement

High resolution versions of all figures, geochemical data (XRF raw data and reference analyses) and SEM-BSE and EDS maps (incl. mineral maps, element concentration heat maps, and tabulated chemical composition of each raster point) of the samples are available in the Open Science Framework repository Bamberg, B. (2023, June 28). Basaltic Fault Rock Petrology. Retrieved from osf.io/r3skf.

883 Table 1. Bulk rock composition (major elements) of selected fault rock samples in weight
884 percent, recalculated to 100 % (incl. LOI). Raw data in data repository (Bamberg, 2023).
885 Cc – cataclasite, cal – calcite, DZ – damage zone, FW – foot wall, HW – hanging wall,
886 LLD – lower limit of detection, RSD – relative standard deviation, vein – fault vein,
887 zeo – zeolite.
888

Sample	Rock Type	SiO_2	TiO_2	Al_2O_3	Fe_2O_3	MnO	MgO	CaO	Na_2O	K_2O	P_2O_5	SO_3	LOI
GOT13	**host**	47.60	2.68	13.54	13.21	0.17	6.52	10.61	2.28	0.22	0.22	0.10	2.85
GOT34	**HW DZ**	46.06	2.92	11.21	14.19	0.17	6.92	8.97	2.15	0.35	0.24	0.10	6.71
GOT21	**FW DZ**	49.68	2.12	14.43	11.79	0.11	4.71	7.46	2.77	1.11	0.20	0.10	5.52
GOT22	**breccia**	49.04	2.32	12.05	11.03	0.20	5.04	8.66	1.06	0.41	0.20	0.10	9.90
GOT31	**proto-cc**	55.27	1.65	14.85	9.73	0.15	2.92	12.15	0.75	0.22	0.17	0.10	2.03
GOT33	**cc**	47.11	1.66	15.53	8.73	0.11	4.24	11.57	1.45	0.47	0.16	0.10	8.87
GOT20	**cc**	53.06	1.37	13.84	7.48	0.07	3.01	7.23	0.84	0.25	0.12	0.10	12.62
GOT5cc	**ultra-cc**	48.91	1.98	13.47	10.08	0.16	4.38	9.05	0.93	0.29	0.17	0.10	10.49
GOT26	**ultra-cc**	46.69	2.31	13.64	11.88	0.20	5.39	9.79	1.46	0.32	0.20	0.10	8.03
GOT23	**zeo vein**	57.82	0.24	17.06	1.28	0.02	0.36	8.17	1.38	0.05	0.02	0.10	13.50
GOT5v	**zeo vein**	48.98	0.45	12.89	2.27	0.04	0.59	14.86	0.56	0.06	0.06	0.10	19.14
GOT12	**cal vein**	11.29	0.36	2.67	2.31	0.09	0.57	45.94	0.12	0.05	0.05	0.10	36.44
IBOhwhost	**HW host**	47.00	3.76	12.78	16.92	0.24	5.36	9.51	2.72	0.35	0.38	0.10	0.88
IBOfwhost	**FW host**	47.09	3.28	13.59	15.94	0.21	5.18	9.49	3.24	0.75	0.33	0.10	0.79
IBO1-4	**breccia**	39.97	2.64	9.98	14.72	0.16	5.16	12.32	1.82	0.58	0.26	0.10	12.28
IBO1-3	**proto-cc**	47.03	3.35	13.11	15.98	0.20	4.87	9.93	2.95	0.70	0.33	0.10	1.45
IBO1-1	**cc**	28.03	1.15	7.92	6.89	0.13	1.39	25.27	1.28	1.36	0.08	0.02	26.47
IBO1-5	**gouge**	46.86	3.33	13.14	16.16	0.20	4.96	9.91	2.95	0.68	0.33	0.10	1.39
SEL2	**host**	47.59	2.90	14.78	12.15	0.24	5.47	8.88	1.76	0.35	0.24	0.10	5.54
SEL3	**DZ cc**	44.74	2.38	16.91	9.68	0.11	3.48	9.42	1.92	0.23	0.22	0.10	10.80
SEL1	**ultra-cc**	44.61	1.87	14.44	10.43	0.16	5.48	10.97	1.76	0.30	0.17	0.01	9.80
LLD		0.40	0.01	0.28	0.02	0.01	0.13	0.05	0.17	0.01	0.02	0.08	
RSD / %		0.6	0.4	1.5	0.3	49.4	0.3	0.3	3.2	1.5	2.0	48.3	

889

890

Table 2. Fluid composition in Iceland, Hawaii, and the Deccan Traps. All concentrations are in ppm.

		temp. / °C	pH	HCO_3	CO_2	SiO_2	Ca	Na	Mg	K
Iceland										
Snaefellsnes cold water springs	*Arnórsson & Barnes, 1983*	4-6	4.5-6.2		616-4100	5-77	2-256	5-660	1-178	0-27
NE Iceland spring water	*Gislason & Eugster, 1987b*	2-34	7.7-10.2		18-85	12-93	1-74	89-193	0-22	0-10
High-temp. geothermal waters	*Arnórsson, 1995a*	181-340	5.3-7.2		154-15534	271-664	0-1467	76-9594	0-1	6-1480
Low-temp. geothermal waters	*Arnórsson, 1995b*	7-147	6.1-10.6		1.7-1358	21-182	1-560	9-486	0-21	0-37
SW Iceland geothermal	*Aggarwal et al., 2000*	7-92	6.2-10.7		11-1101					
Hawaii										
Kilauea summit borehole (NSF)	*Tilling & Jones, 1991*		7.6-8.7	150-1080	20-35	67-180	36-106	214-769	22-110	43-142
Hawaii flank borehole (KP-1)	*Thomas et al., 1996*		7.5-7.9	61-140		9-39	76-478	1740-11700	224-1320	67-398
Kilauea summit borehole (NSF)	*Hurwitz et al., 2003*	73-92	6.7-8.7			107-173	77-162	548-838	366-737	151-245
Deccan Traps										
Jalna groundwater	*Kale et al., 2021*	21-32	7.0-9.0	182-970			5-54	34-261	2-46	0-21

Table 3. Mass balance calculation for SiO_2 across a section of the Gøtugjógv fault zone using equation 3.3. SiO_2 is leached from the far damage zone and enriched in the near damage zone and fault core. Summing the mass change factors ($\boldsymbol{T_{SiO_2}}$) in the enriched subzones weighted by the subzones' width ($\boldsymbol{W}$) gives the total amount of SiO_2 that has been mobilized ($\boldsymbol{M_{SiO_2}}$; left-hand table). Dividing this by the mass change factor in the depleted far damage zone yields the width of leached damage zone required to balance SiO_2 redistribution (11.97 m; right-hand table). Cal – calcite, DZ – damage zone, zeo – zeolite.

SiO_2 enrichment in

structure	**sample**	$\boldsymbol{T_{SiO_2} \times W / m}$		$\boldsymbol{= M_{SiO_2}}$
near DZ	GOT21	0.29	0.30	0.09
breccia	GOT22	0.31	1.50	0.46
protocataclasite	GOT31	1.29	0.10	0.13
cataclasite	GOT33	1.39	0.05	0.07
cataclasite	GOT5cc	0.44	0.30	0.13
ultracataclasite	GOT26	0.21	0.05	0.01
zeo vein	GO5Tv	5.08	0.05	0.25
cal vein	GOT12	0.59	0.05	0.03
Total			2.40	**1.17**

→

SiO_2 leaching from

structure	**sample**	**Total $\boldsymbol{M_{SiO_2} / T_{SiO_2}}$**		$\boldsymbol{= W / m}$
far DZ	GOT34	**1.17**	-0.10	**-11.97**

References

Agar, S. M., 1990, Fracture evolution in the upper ocean crust: evidence from DSDP hole 504B: Geological Society, London, Special Publications, v. 54, no. 1, p. 41-50, doi:10.1144/GSL.SP.1990.054.01.04.

Aggarwal, J., Palmer, M., Bullen, T., Arnórsson, S., and Ragnarsdóttir, K., 2000, The boron isotope systematics of Icelandic geothermal waters: 1. Meteoric water charged systems: Geochimica et Cosmochimica Acta, v. 64, no. 4, p. 579-585, https://doi.org/10.1016/S0016-7037(99)00300-2.

Ague, J. J., 1991, Evidence for major mass transfer and volume strain during regional metamorphism of pelites: Geology, v. 19, no. 8, p. 855-858, https://doi.org/10.1130/0091-7613(1991)019%3C0855:EFMMTA%3E2.3.CO;2.

Alt, J. C., and Honnorez, J., 1984, Alteration of the upper oceanic crust, DSDP site 417: mineralogy and chemistry: Contributions to Mineralogy and petrology, v. 87, no. 2, p. 149-169, https://doi.org/10.1007/BF00376221.

Arnórsson, S., 1995a, Geothermal systems in Iceland: Structure and conceptual models—I. High-temperature areas: Geothermics, v. 24, no. 5, p. 561-602, https://doi.org/10.1016/0375-6505(95)00025-9.

-, 1995b, Geothermal systems in Iceland: Structure and conceptual models—II. Low-temperature areas: Geothermics, v. 24, no. 5, p. 603-629, https://doi.org/10.1016/0375-6505(95)00026-7.

Arnórsson, S., and Barnes, I., 1983, The nature of carbon dioxide waters in Snaefellsnes, western Iceland: Geothermics, v. 12, no. 2-3, p. 171-176, https://doi.org/10.1016/0375-6505(83)90027-5.

Bamberg, B., 2023, Basaltic Fault Rock Petrology: Open Science Framework, https://osf.io/r3skf.

Bamberg, B., Walker, R., Reichow, M., and Ougier-Simonin, A., 2022, Fluid-driven cyclic reorganization in shallow basaltic fault zones: Geosphere, https://doi.org/10.1130/ges02488.1.

Bindeman, I. N., and Davis, A. M., 2000, Trace element partitioning between plagioclase and melt: investigation of dopant influence on partition behavior: Geochimica et Cosmochimica Acta, v. 64, no. 16, p. 2863-2878, https://doi.org/10.1016/S0016-7037(00)00389-6.

Boschi, C., Früh-Green, G. L., Delacour, A., Karson, J. A., and Kelley, D. S., 2006, Mass transfer and fluid flow during detachment faulting and development of an oceanic core complex, Atlantis Massif (MAR 30°N): Geochemistry, Geophysics, Geosystems, v. 7, no. 1, https://doi.org/10.1029/2005GC001074.

Boulton, C., Moore, D. E., Lockner, D. A., Toy, V. G., Townend, J., and Sutherland, R., 2014, Frictional properties of exhumed fault gouges in DFDP-1 cores, Alpine Fault, New Zealand: Geophysical Research Letters, v. 41, no. 2, p. 356-362, https://doi.org/10.1002/2013GL058236.

Bubeck, A., Walker, R. J., Imber, J., Holdsworth, R. E., MacLeod, C. J., and Holwell, D. A., 2017, Extension parallel to the rift zone during segmented fault growth: application to the evolution of the NE Atlantic: Solid Earth, v. 8, p. 1161-1180, https://doi.org/10.5194/se-8-1161-2017.

Carpenter, B. M., Ikari, M. J., and Marone, C., 2016, Laboratory observations of time-dependent frictional strengthening and stress relaxation in natural and synthetic fault gouges: Journal of Geophysical Research: Solid Earth, v. 121, no. 2, p. 1183-1201, https://doi.org/10.1002/2015JB012136.

Chalmers, J. A., and Waagstein, R., 2006, Scientific results from the deepened Lopra-1 borehole, Faroe Islands, Geological Survey of Denmark and Greenland, Danish Ministry of the Environment.

D'Antonio, M., and Kristensen, M., 2005, Hydrothermal alteration of oceanic crust in the West Philippine Sea Basin (Ocean Drilling Program Leg 195, Site 1201): inferences from a mineral chemistry investigation: Mineralogy and Petrology, v. 83, no. 1, p. 87-112, https://doi.org/10.1007/s00710-004-0060-6.

Das, A., and Krishnaswami, S., 2006, Barium in Deccan Basalt Rivers: its abundance, relative mobility and flux: Aquatic Geochemistry, v. 12, no. 3, p. 221-238, https://doi.org/10.1007/s10498-005-5856-4.

Deer, W. A., FRS, Howie, R. A., and Zussman, J., 2013, An Introduction to the Rock-Forming Minerals, Mineralogical Society of Great Britain and Ireland.

Eidesgaard, Ó. R., Schovsbo, N. H., Boldreel, L. O., and Ólavsdóttir, J., 2019, Shallow geothermal energy system in fractured basalt: A case study from Kollafjørður, Faroe Islands, NE-Atlantic Ocean: Geothermics, v. 82, p. 296-314, https://doi.org/10.1016/j.geothermics.2019.07.005.

Frolova, J., Ladygin, V., Rychagov, S., and Zukhubaya, D., 2014, Effects of hydrothermal alterations on physical and mechanical properties of rocks in the Kuril–Kamchatka island arc: Engineering Geology, v. 183, p. 80-95, https://doi.org/10.1016/j.enggeo.2014.10.011.

Gaina, C., Gernigon, L., and Ball, P., 2009, Palaeocene–Recent plate boundaries in the NE Atlantic and the formation of the Jan Mayen microcontinent: Journal of the Geological Society, v. 166, no. 4, p. 601, https://doi.org/10.1144/0016-76492008-112.

959 Gariépy, C., Ludden, J., and Brooks, C., 1983, Isotopic and trace element constraints on the genesis of the Faeroe lava
960 pile: Earth and Planetary Science Letters, v. 63, no. 2, p. 257-272, https://doi.org/10.1016/0012-
961 821X(83)90041-9.
962 Gernigon, L., Gaina, C., Olesen, O., Ball, P., Péron-Pinvidic, G., and Yamasaki, T., 2012, The Norway Basin revisited:
963 From continental breakup to spreading ridge extinction: Marine and Petroleum Geology, v. 35, no. 1, p. 1-
964 19, https://doi.org/10.1016/j.marpetgeo.2012.02.015.
965 Ghiara, M., Franco, E., Petti, C., Stanzione, D., and Valentino, G., 1993, Hydrothermal interaction between basaltic
966 glass, deionized water and seawater: Chemical Geology, v. 104, no. 1-4, p. 125-138,
967 https://doi.org/10.1016/0009-2541(93)90146-A.
968 Ghiara, M. R., Petti, C., Franco, E., Lonis, R., Luxoro, S., and Gnazzo, L., 1999, Occurrence of clinoptilolite and
969 mordenite in Tertiary calc-alkaline pyroclastites from Sardinia (Italy): Clays and Clay Minerals, v. 47, no. 3,
970 p. 319-328, https://doi.org/10.1346/CCMN.1999.0470308.
971 Ghiorso, M. S., and Sack, R. O., 1995, Chemical mass transfer in magmatic processes IV. A revised and internally
972 consistent thermodynamic model for the interpolation and extrapolation of liquid-solid equilibria in
973 magmatic systems at elevated temperatures and pressures: Contributions to Mineralogy and Petrology, v.
974 119, no. 2, p. 197-212, https://doi.org/10.1007/BF00307281.
975 Gislason, S. R., and Eugster, H. P., 1987a, Meteoric water-basalt interactions. I: A laboratory study: Geochimica et
976 Cosmochimica Acta, v. 51, no. 10, p. 2827-2840, https://doi.org/10.1016/0016-7037(87)90161-X.
977 -, 1987b, Meteoric water-basalt interactions. II: A field study in NE Iceland: Geochimica et Cosmochimica Acta, v.
978 51, no. 10, p. 2841-2855, https://doi.org/10.1016/0016-7037(87)90162-1.
979 Govindaraju, K., 1994, 1994 Compilation of working values and sample description for 383 geostandards:
980 Geostandards Newsletter, v. 18, no. S1, p. 1-158, https://doi.org/10.1046/j.1365-2494.1998.53202081.x-i1.
981 Grant, J. A., 1986, The isocon diagram; a simple solution to Gresens' equation for metasomatic alteration: Economic
982 Geology, v. 81, no. 8, p. 1976-1982, https://doi.org/10.2113/gsecongeo.81.8.1976.
983 Gratier, J. P., Renard, F., and Vial, B., 2014, Postseismic pressure solution creep: Evidence and time-dependent change
984 from dynamic indenting experiments: Journal of Geophysical Research: Solid Earth, v. 119, no. 4, p. 2764-
985 2779, https://doi.org/10.1002/2013JB010768.
986 Gualda, G. A. R., and Ghiorso, M. S., 2015, MELTS_Excel: A Microsoft Excel-based MELTS interface for research
987 and teaching of magma properties and evolution: Geochemistry, Geophysics, Geosystems, v. 16, no. 1, p.
988 315-324, https://doi.org/10.1002/2014GC005545.
989 Gualda, G. A. R., Ghiorso, M. S., Lemons, R. V., and Carley, T. L., 2012, Rhyolite-MELTS: a Modified Calibration
990 of MELTS Optimized for Silica-rich, Fluid-bearing Magmatic Systems: Journal of Petrology, v. 53, no. 5, p.
991 875-890, https://doi.org/10.1093/petrology/egr080.
992 Hadizadeh, J., 1994, Interaction of cataclasis and pressure solution in a low-temperature carbonate shear zone: Pure
993 and Applied Geophysics, v. 143, no. 1, p. 255-280, https://doi.org/10.1007/BF00874331.
994 Haines, S. H., Kaproth, B., Marone, C., Saffer, D., and van der Pluijm, B., 2013, Shear zones in clay-rich fault gouge:
995 A laboratory study of fabric development and evolution: Journal of Structural Geology, v. 51, p. 206-225,
996 https://doi.org/10.1016/j.jsg.2013.01.002.
997 Hald, N., and Waagstein, R., 1991, The dykes and sills of the Early Tertiary Faeroe Island basalt plateau: Transactions
998 of the Royal Society of Edinburgh: Earth Sciences, v. 82, no. 4, p. 373-388,
999 https://doi.org/10.1017/S0263593300004211.
1000 Hansen, H., Pedersen, A., Duncan, R., Bird, D., Brooks, C., Fawcett, J., Gittins, J., Gorton, M., and O'Day, P., 2002,
1001 Volcanic stratigraphy of the southern Prinsen af Wales Bjerge region, East Greenland: Geological Society,
1002 London, Special Publications, v. 197, no. 1, p. 183-218, https://doi.org/10.1144/GSL.SP.2002.197.01.08.
1003 Hawkins, D. B., 1981, Kinetics of glass dissolution and zeolite formation under hydrothermal conditions: Clays and
1004 Clay Minerals, v. 29, no. 5, p. 331-340, https://doi.org/10.1346/CCMN.1981.0290503.
1005 Hayman, N. W., and Karson, J. A., 2007, Faults and damage zones in fast-spread crust exposed on the north wall of
1006 the Hess Deep Rift: Conduits and seals in seafloor hydrothermal systems: Geochemistry, Geophysics,
1007 Geosystems, v. 8, no. 10, https://doi.org/10.1029/2007GC001623.
1008 -, 2009, Crustal faults exposed in the Pito Deep Rift: Conduits for hydrothermal fluids on the southeast Pacific Rise:
1009 Geochemistry, Geophysics, Geosystems, v. 10, no. 2, https://doi.org/10.1029/2008GC002319.
1010 Hippertt, J., 1998, Breakdown of feldspar, volume gain and lateral mass transfer during mylonitization of granitoid in
1011 a low metamorphic grade shear zone: Journal of Structural Geology, v. 20, no. 2-3, p. 175-193,
1012 https://doi.org/10.1016/S0191-8141(97)00083-7.
1013 Hjartarson, A., and Armannsson, H., Geothermal research in Greenland, *in* Proceedings World Geothermal Congress,
1014 Bali, Indonesia,°2010, p. 1-8.

1015 Holm, P. M., Hald, N., and Waagstein, R., 2001, Geochemical and Pb–Sr–Nd isotopic evidence for separate hot
1016 depleted and Iceland plume mantle sources for the Paleogene basalts of the Faroe Islands: Chemical Geology,
1017 v. 178, no. 1-4, p. 95-125, https://doi.org/10.1016/S0009-2541(01)00260-1.
1018 Hurwitz, S., Goff, F., Janik, C. J., Evans, W. C., Counce, D. A., Sorey, M. L., and Ingebritsen, S. E., 2003, Mixing of
1019 magmatic volatiles with groundwater and interaction with basalt on the summit of Kilauea Volcano, Hawaii:
1020 Journal of Geophysical Research: Solid Earth, v. 108, no. B1, https://doi.org/10.1029/2001JB001594.
1021 Imai, N., Terashima, S., Itoh, S., and Ando, A., 1995, 1994 Compialtion of analytical data for minor and trace elements
1022 in seventeen GSJ geochemical reference samples, "Igneous Rock Series": Geostandards Newsletter, v. 19,
1023 no. 2, p. 135-213, https://doi.org/10.1111/j.1751-908X.1995.tb00158.x.
1024 Jørgensen, O., 2006, The regional distribution of zeolites in the basalts of the Faroe Islands and the significance of
1025 zeolites as palaeotemperature indicators: Geological Survey of Denmark and Greenland Bulletin, v. 9, p.
1026 123-156, https://doi.org/10.34194/geusb.v9.4865.
1027 Kale, A., Bandela, N., Kulkarni, J., Sahoo, S. K., and Kumar, A., 2021, Hydrogeochemistry and multivariate statistical
1028 analysis of groundwater quality of hard rock aquifers from Deccan trap basalt in Western India:
1029 Environmental Earth Sciences, v. 80, no. 7, p. 1-24, https://doi.org/10.1007/s12665-021-09586-7.
1030 Kristmannsdóttir, H., 1979, Alteration of Basaltic Rocks by Hydrothermal-Activity at 100-300 °C, Developments in
1031 Sedimentology, Volume 27, Elsevier, p. 359-367.
1032 Kristmannsdóttir, H., and Tomasson, J., 1978, Zeolite Zones In Geothermal Areas in Iceland, *in* L.B. Sand, F. A. M.,
1033 ed., Natural Zeolites: Occurrence, Properties, Use: Elmsford, New York, Pergamon Press, p. 277-284.
1034 Lewis, A. L., Sarkar, B., Wade, P., Kemp, S. J., Hodson, M. E., Taylor, L. L., Yeong, K. L., Davies, K., Nelson, P.
1035 N., Bird, M. I., Kantola, I. B., Masters, M. D., DeLucia, E., Leake, J. R., Banwart, S. A., and Beerling, D. J.,
1036 2021, Effects of mineralogy, chemistry and physical properties of basalts on carbon capture potential and
1037 plant-nutrient element release via enhanced weathering: Applied Geochemistry, v. 132, p. 105023,
1038 https://doi.org/10.1016/j.apgeochem.2021.105023.
1039 Marieni, C., Přikryl, J., Aradóttir, E. S., Gunnarsson, I., and Stefánsson, A., 2018, Towards 'green'geothermal energy:
1040 Co-mineralization of carbon and sulfur in geothermal reservoirs: International Journal of Greenhouse Gas
1041 Control, v. 77, p. 96-105, https://doi.org/10.1016/j.ijggc.2018.07.011.
1042 Matter, J. M., Stute, M., Snæbjörnsdottir, S. Ó., Oelkers, E. H., Gislason, S. R., Aradottir, E. S., Sigfusson, B.,
1043 Gunnarsson, I., Sigurdardottir, H., Gunnlaugsson, E., Axelsson, G., Alfredsson, H. A., Wolff-Boenisch, D.,
1044 Mesfin, K., Taya, D. F. D. L. R., Hall, J., Dideriksen, K., and Broecker, W. S., 2016, Rapid carbon
1045 mineralization for permanent disposal of anthropogenic carbon dioxide emissions: Science, v. 352, no. 6291,
1046 p. 1312-1314, http://doig.org/10.1126/science.aad8132.
1047 Mattioli, M., Cenni, M., and Passaglia, E., 2016, Secondary mineral assemblages as indicators of multi stage alteration
1048 processes in basaltic lava flows: Evidence from the Lessini Mountains, Veneto Volcanic Province, Northern
1049 Italy: Periodico di Mineralogia, v. 85, p. 1-24, https://doi.org/10.2451/2015PM0375.
1050 McInerney, F. A., and Wing, S. L., 2011, The Paleocene-Eocene Thermal Maximum: A perturbation of carbon cycle,
1051 climate, and biosphere with implications for the future: Annual Review of Earth and Planetary Sciences, v.
1052 39, p. 489-516, https://doi.org/10.1146/annurev-earth-040610-133431.
1053 Neuhoff, P. S., Fridriksson, T., and Bird, D. K. J. I. G. R., 2000, Zeolite parageneses in the north Atlantic igneous
1054 province: Implications for geotectonics and groundwater quality of basaltic crust, v. 42, no. 1, p. 15-44,
1055 https://doi.org/10.1080/00206810009465068.
1056 Passey, S., 2009, Recognition of a faulted basalt lava flow sequence through the correlation of stratigraphic marker
1057 units, Skopunarfjørður, Faroe Islands, *in* Varming, T., and Ziska, H., eds., Faroe Islands Exploration
1058 Conference: Proceedings of the 2nd Conference, Volume 50: Faroe Islands, Annales Societatis Scientiarum
1059 Færoensis, p. 174-204.
1060 Passey, S. R., and Bell, B. R., 2007, Morphologies and emplacement mechanisms of the lava flows of the Faroe Islands
1061 Basalt Group, Faroe Islands, NE Atlantic Ocean: Bulletin of Volcanology, v. 70, no. 2, p. 139-156,
1062 https://doi.org/10.1007/s00445-007-0125-6.
1063 Passey, S. R., and Jolley, D. W., 2008, A revised lithostratigraphic nomenclature for the Palaeogene Faroe Islands
1064 Basalt group, NE Atlantic Ocean: Earth and Environmental Science Transactions of the Royal Society of
1065 Edinburgh, v. 99, no. 3-4, p. 127-158, https://doi.org/10.1017/S1755691009008044.
1066 Philpotts, J. A., and Schnetzler, C. C., 1970, Phenocryst-matrix partition coefficients for K, Rb, Sr and Ba, with
1067 applications to anorthosite and basalt genesis: Geochimica et Cosmochimica Acta, v. 34, no. 3, p. 307-322,
1068 https://doi.org/10.1016/0016-7037(70)90108-0.

Proctor, B., Lockner, D., Kilgore, B., Mitchell, T., and Beeler, N., 2020, Direct evidence for fluid pressure, dilatancy, and compaction affecting slip in isolated faults: Geophysical Research Letters, v. 47, no. 16, p. e2019GL086767, https://doi.org/10.1029/2019GL086767.

Pytte, A., and Reynolds, R., 1989, The thermal transformation of smectite to illite, Thermal history of sedimentary basins, Springer, p. 133-140.

Rasmussen, J., and Noe-Nygaard, A., 1970, Geology of the Faeroe Islands: (Pre-Quaternary), Copenhagen, CA Reitzels.

Ritchie, J., and Hitchen, K., 1996, Early Paleogene offshore igneous activity to the northwest of the UK and its relationship to the North Atlantic Igneous Province: Geological Society, London, Special Publications, v. 101, no. 1, p. 63-78, https://doi.org/10.1144/GSL.SP.1996.101.01.04.

Schenato, F., Formoso, M., Dudoignon, P., Meunier, A., Proust, D., and Mas, A., 2003, Alteration processes of a thick basaltic lava flow of the Paraná Basin (Brazil): petrographic and mineralogical studies: Journal of South American Earth Sciences, v. 16, no. 5, p. 423-444, https://doi.org/10.1016/S0895-9811(03)00098-1.

Shimamoto, T., and Logan, J. M., 1981, Effects of simulated fault gouge on the sliding behavior of Tennessee sandstone: nonclay gouges: Journal of Geophysical Research: Solid Earth, v. 86, no. B4, p. 2902-2914, https://doi.org/10.1029/JB086iB04p02902.

Snæbjörnsdóttir, S. Ó., Sigfússon, B., Marieni, C., Goldberg, D., Gislason, S. R., and Oelkers, E. H., 2020, Carbon dioxide storage through mineral carbonation: Nature Reviews Earth & Environment, v. 1, no. 2, p. 90-102, https://doi.org/10.1038/s43017-019-0011-8.

Søager, N., and Holm, P. M., 2009, Extended correlation of the Paleogene Faroe Islands and East Greenland plateau basalts: Lithos, v. 107, no. 3-4, p. 205-215, https://doi.org/10.1016/j.lithos.2008.10.002.

-, 2011, Changing compositions in the Iceland plume; Isotopic and elemental constraints from the Paleogene Faroe flood basalts: Chemical Geology, v. 280, no. 3-4, p. 297-313, https://doi.org/10.1016/j.chemgeo.2010.11.017.

Stillings, M., Shipton, Z. K., and Lunn, R. J., 2023, Mechanochemical processing of silicate rocks to trap CO2: Nature Sustainability, 10.1038/s41893-023-01083-y.

Storey, M., Duncan, R. A., and Tegner, C., 2007, Timing and duration of volcanism in the North Atlantic Igneous Province: Implications for geodynamics and links to the Iceland hotspot: Chemical Geology, v. 241, no. 3, p. 264-281, https://doi.org/10.1016/j.chemgeo.2007.01.016.

Thomas, D., Paillet, F. L., and Conrad, M., 1996, Hydrogeology of the Hawaii Scientific Drilling Project borehole KP-1: 2. Groundwater geochemistry and regional flow patterns: Journal of Geophysical Research: Solid Earth, v. 101, no. B5, p. 11683-11694, https://doi.org/10.1029/95JB03845.

Tilling, R. I., and Jones, B. F., 1991, Composition of waters from the research drill hole at summit of Kilauea Volcano and of selected thermal and non-thermal groundwaters, Hawaii.

Triana, R., Manuel, J., Herrera, R., Francisco, J., Ríos, R., Alberto, C., Castellanos, A., Mauricio, O., Henao, M., and Antonio, J., 2012, Natural zeolites filling amygdales and veins in basalts from the British Tertiary Igneous Province on the Isle of Skye, Scotland: Earth Sciences Research Journal, v. 16, no. 1, p. 41-53.

Varga, L. B., Varga, R. J., and Schiffman, P., 1992, Relation between ore-forming hydrothermal systems and extensional deformation in the Solea graben spreading center, Troodos ophiolite, Cyprus: Geology, v. 20, no. 11, p. 987-990, https://doi.org/10.1130/0091-7613(1992)020<0987:Rbofhs>2.3.Co;2.

Velde, B., and Vasseur, G., 1992, Estimation of the diagenetic smectite to illite transformation in time-temperature space: American Mineralogist, v. 77, no. 9-10, p. 967-976.

Waagstein, R., Guise, P., and Rex, D. J. G. S., London, Special Publications, 2002, K/Ar and 39Ar/40Ar whole-rock dating of zeolite facies metamorphosed flood basalts: the upper Paleocene basalts of the Faroe Islands, NE Atlantic, v. 197, no. 1, p. 219-252, https://doi.org/10.1144/GSL.SP.2002.197.01.09.

Waagstein, R., Hald, N., Jørgensen, O., Nielsen, P. H., Noe, A., Jørgensen, O., Noe-Nygaard, A., and Schonharting, G., 1984, Deep drilling on the Faeroe Islands: Bulletin of the Geological Society of Denmark, v. 32, p. 133-138.

Walker, R. J., Holdsworth, R. E., Armitage, P. J., and Faulkner, D. R., 2013a, Fault zone permeability structure evolution in basalts: Geology, v. 41, no. 1, p. 59-62, https://doi.org/10.1130/G33508.1.

Walker, R. J., Holdsworth, R. E., Imber, J., and Ellis, D., 2011, Onshore evidence for progressive changes in rifting directions during continental break-up in the NE Atlantic: Journal of the Geological Society, v. 168, no. 1, p. 27-48, https://doi.org/10.1144/0016-76492010-021.

Walker, R. J., Holdsworth, R. E., Imber, J., and Ellis, D., 2012, Fault-zone evolution in layered basalt sequences: A case study from the Faroe Islands, NE Atlantic margin: GSA Bulletin, v. 124, no. 7-8, p. 1382-1393, https://doi.org/10.1130/B30512.1.

Walker, R. J., Holdsworth, R. E., Imber, J., Faulkner, D. R., and Armitage, P. J., 2013b, Fault zone architecture and fluid flow in interlayered basaltic volcaniclastic-crystalline sequences: Journal of Structural Geology, v. 51, p. 92-104, https://doi.org/10.1016/j.jsg.2013.03.004.

Winter, J., 2001, An introduction to igneous and metamorphic petrology, Pearson, v. 552.1 W 784552.1 W 784552.1 W 784552.1 W 784.

Woodcock, N. H., and Mort, K., 2008, Classification of fault breccias and related fault rocks: Geological Magazine, v. 145, no. 3, p. 435-440, https://doi.org/10.1017/S0016756808004883.

Yukselen-Aksoy, Y., 2010, Characterization of two natural zeolites for geotechnical and geoenvironmental applications: Applied Clay Science, v. 50, no. 1, p. 130-136, https://doi.org/10.1016/j.clay.2010.07.015.

Zen, E.-A., 1961, The zeolite facies; an interpretation: American Journal of Science, v. 259, no. 6, p. 401-409, https://doi.org/10.2475/ajs.259.6.401.

Zihlmann, B., Müller, S., Coggon, R. M., Koepke, J., Garbe-Schönberg, D., and Teagle, D. A. H., 2018, Hydrothermal fault zones in the lower oceanic crust: An example from Wadi Gideah, Samail ophiolite, Oman: Lithos, v. 323, p. 103-124, https://doi.org/10.1016/j.lithos.2018.09.008.

Zviagina, B. B., Drits, V. A., and Dorzhieva, O. V., 2020, Distinguishing Features and Identification Criteria for K-Dioctahedral 1M Micas (Illite-Aluminoceladonite and Illite-Glauconite-Celadonite Series) from Middle-Infrared Spectroscopy Data: Minerals, v. 10, no. 2, p. 153.

Geochemistry, Geophysics, Geosystems

Supporting Information for

Petrological Evolution and Mass Redistribution in Basaltic Fault Zones: An Example from the Faroe Islands, North Atlantic Igneous Province

Bob Bamberg[1], Marc K. Reichow[1], Richard J. Walker[2], Audrey Ougier-Simonin[3]

[1]School of Geography, Geology and the Environment, University of Leicester, University Road, Leicester LE1 7RH, UK

[2]Department of Earth and Planetary Sciences, University of California, Davis, 1 Shields Avenue, Davis, California 95616, USA

[3]Rock Mechanics and Physics Laboratory, British Geological Survey, Nicker Hill, Keyworth, Nottingham NG21 5GG, UK

Contents of this file

Introduction

This document contains a description of the methods used for mineral classification based on scanning electron microscopy - energy dispersive spectroscopy (SEM-EDS) and X-ray fluorescence (XRF) spectroscopy. This is followed by a brief quality discussion of automated mineral classification based on SEM-EDS, including a comparison of SEM-EDS chemistry to XRF chemistry (Figure S1).

Tables include the classification scheme used for automated phase identification (Table S1), XRF trace element composition of our samples (Table S2), XRF major element composition of reference material (Table S3) and blank analysis (Table S4), and XRF trace element composition for reference materials (Table S5). Additionally, isocon plots for all samples are provided (Figures S2–S4), and a 1D mass balance estimation for CaO, Al_2O_3, and SiO_2 across the Gøtugjógv fault zone (Table S6).

Methods

Automated phase identification and microtexture imaging were performed on a ZEISS Sigma 300 Field emission - analytical scanning electron microscope (SEM). Polished and carbon-coated (ca. 30 nm) thin sections were analyzed under high vacuum (ca. 1.0 × 10-5 Pa) using a 15 kV accelerating voltage (suitable for silicate minerals) and a 120 µm beam aperture. Imagery was captured via a high-definition backscattered electron detector (BSE). Chemical composition was determined via energy dispersive X-Ray spectrometry (EDS) utilizing two Bruker XFlash|60 EDS detectors, that are positioned perpendicular to one another to prevent data shadowing effects, with a 1.25 µm beam step and a dwell time of 8 µs. The chemical compositions were calculated using a standardless P/B-ZAF quantification method via Bruker Esprit 2.1. Element concentration data are only semi-quantitative as no reference material was used for calibration. Automated phase identification was performed using ZEISS Mineralogic software. The chemical composition of each analysis (i.e., pixel) is compared to the compositional ranges in a user-defined, hierarchical phase list (recipe; see Table S1), and assigned the first matching phase. Phase selection and compositional ranges for this recipe are based on literature review and petrographic characterization, and are improved in an iterative process to match the phase compositions in the samples. The process is similar to manual phase identification in SEM-EDS data, but automatically applied to the whole dataset.

Whole rock geochemistry was determined using a PANanalytical Axios Advanced wavelength dispersive X-ray fluorescence spectrometer. Major element and volatile concentration was determined in fusion beads prepared from ignited powders with a sample to flux ratio of 1/5. Loss on ignition (LOI) was determined after ignition at 950 °C in air for 1 h of the pre-dried powders. Trace elements were measured in pressed powder pellets with 7.5 g sample material bound with 15–20 drops polyvinyl alcohol. Detection limits for major elements, as defined from blank analysis, are usually better than 0.1 wt.%. Calibrations were set using a suite of 9 international and internal rock reference materials for major elements and 17 reference materials for trace elements (data provided in data repository Bamberg, 2023). Analytical uncertainties of XRF data are between 0.3 and 3.2 % for major elements, except for MnO (49.4 %) and SO3 (48.3 %), and 0.2–8.2 % for trace elements. Major and trace element analytical results for the Faroe Island samples are provided in Table 1 (main paper) and Table S2 and selected reference materials in Table S3 to Table S5.

Limitations of Automated Phase Identification using SEM-EDS

Although a powerful tool for rapid mineral identification and classification, automated phase identification based on EDS chemical analysis is subject to the same limitations as manual mineral identification in SEM spectroscopy. For example, minerals that share near-identical chemical compositions, such as Fe-Mg-illite and celadonite, are indistinguishable using this method despite being easily distinguished optically. This is prominently illustrated in the lining of amygdales (Figure 5G & Figure 6C). Furthermore, owing to the small grain size of some of the samples (e.g., cataclasites) and secondary phases, individual measurements (i.e., data points, or pixel) can reflect the superposed spectra of more than one phase contained in the interaction volume of the X-rays, measuring a few micrometers across. We refer to such measurements as a 'mixel' (a portmanteau for mixed pixel). These measurements are sometimes misclassified, but more often cannot be matched to one of the predefined mineral phases and remain unclassified. These limitations demand that the compositional ranges for mineral classification (i.e., the mineral recipe) be defined in a way that balances the

proportion of measurements that can be classified (wider ranges) against the proportion of misclassified measurements (smaller ranges).

Automated phase identification in the host rock and damage zone generally agrees well with our petrographic observations. Plagioclase and pyroxene grain boundaries in mineral maps coincide with grain boundaries identified in BSE micrographs, whereas zeolites and clay minerals tend to be mapped only partially. In particular, the matrix composition in cataclasites tends to be poorly mapped (Figure 6A & E).

Despite chemical analysis by EDS being performed without calibration to a reference material, the resulting whole rock composition matches well with the whole rock composition measured by XRF (recalculated as element concentration assuming all Fe is Fe2O3) (Figure S1). Significant differences are notable for sample SEL3, which contains large amounts of zeolite, whose constituents are over-reported (by 1.1–2.7 wt.%) at the expense of Fe, Mg, and Ti (by 5.3 wt.%, 2.0 wt.%, and 1.3 wt.%, respectively) in EDS. Overall, Si tends to be over-reported, and O over- or under-reported in EDS compared to XRF. Concentrations of all other elements are generally within 1 wt.% difference between XRF and EDS. Notably, the EDS data is unreliable for elements with low concentrations (e.g., K and Ti) as the accuracy of around 1 wt.% equates to large relative errors (Figure S1). Reliability might be improved by increasing the analytical dwell times.

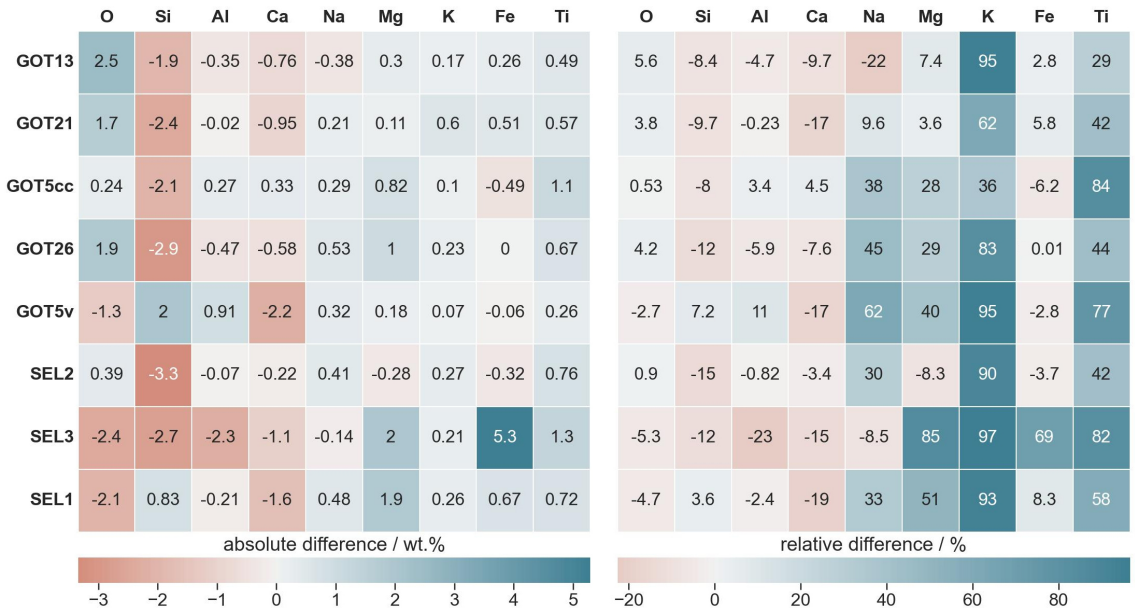

Figure S1. Difference between whole rock chemical composition measured by XRF (assuming full oxidation) and SEM-EDS. The composition from both methods was normalized to the sum of the elements considered here before calculating the difference $\boldsymbol{concentration_{XRF}} - \boldsymbol{concentration_{EDS}}$. Relative difference is normalised to the XRF data.

SEM-EDS Mineralogy

Table S1. Hierarchical list of phase composition used for automated phase classification. The lower bound is indicated by a minus (-) and upper bound by a plus (+) for each element or element ratio. All concentrations are in %.

	Al-	Al+	O-	O+	K-	K+	Si-	Si+	Na-	Na+	Mg-	Mg+	Fe-	Fe+	Ca-	Ca+	Ti-	Ti+	Si/Al-	Si/Al+	(Al+Si)/(Na+Ca)-	(Al+Si)/(Na+Ca)+	(Mg+Ca+Fe)/Si-	(Mg+Ca+Fe)/Si+
Kaolinite	12	40	15	65	0	0.001	15	50	0	1	0	1	0	1	0	1								
Calcite	0	1	33	63			0	1			0	6	0	7	24	70								
Ilmenite	0	10	20	50			0	20					20	55			15	40						
Magnetite	0	10	10	50			0	20					55	80			0	20						
Illite	0	24	30	55	3	12	17	37			0	8	0	20										
Chlorite	1	15	30	60	0	1.9	12	40	0	1	0	25	4	25	0	1								
Pyroxene	0	3	15	50	0	0.01	15	35	0	10	3	24	0.5	30	0	35								1.5
Olivine	0	3	15	50			10	30	0	1	0	40	0	60	0	1							1.5	
Analcime	10	20	30	60			20	40	5	15					0	1								
Montmoril.	8	15	20	65	0	1	15	50	0	6	1	5	0	1	0	12			2					
Saponite	5	10	30	50			15	32	0	1	3	25	8	20	0	8								
Plagioclase	8	22	35	45			18	34	1	11	0	0.01	0	0.01	6	17	0	0.01		4		4.7		
Heulandite	6	13	35	55			27	40	0	1	0	1	0	1	4	12			2.5		4.7	10		
Thomsonite	1	13	20	60			20	40	0	5			0	1	4	15			0.5	1.5		3.5		
Beidellite	10	22	30	52	0	1	15	50	0	7	0	5	0	1	2	14				2	10			
Smectite	6	30	20	65	0	1	15	50	0	5	0	25	1	25	0.01	4								
Zeolite	1	13	20	60			20	40	0	5	0	1	0	1	4	15			1					

X-Ray Fluoresence

Table S2. Bulk rock composition (trace elements) of selected fault rock samples in parts per million. Cc – cataclasite, cal – calcite, DZ – damage zone, FW – foot wall, HW – hanging wall, RSD – relative standard deviation, vein – fault vein, zeo – zeolite.

Sample	Rock Type	Ba	Ce	Co	Cr	Cu	Ga	La	Nb	Nd	Ni	Rb	Sc	Sr	V	Y	Zn	Zr
GOT13	host	38.0	31.8	46.1	237.5	172.6	22.7	8.1	11.3	21.2	98.9	5.3	34.4	221.4	364.1	32.5	102.9	174.9
GOT34	HW DZ	197.2	40.4	47.8	240.8	197.9	17.9	11.0	12.1	25.7	88.8	5.3	35.7	415.1	355.2	34.2	109.3	187.6
GOT21	FW DZ	82.6	29.2	39.6	162.6	141.0	16.4	11.0	9.1	18.4	78.8	22.0	27.6	222.9	297.9	26.7	83.8	141.7
GOT22	breccia	164.3	23.1	38.5	189.7	132.8	17.1	9.4	9.4	15.2	77.8	7.3	29.9	355.6	280.2	24.1	78.1	137.8
GOT31	proto-cc	135.4	19.5	28.4	118.0	83.3	19.7	6.0	6.2	11.9	43.6	4.6	23.4	196.0	242.2	17.3	50.4	85.1
GOT33	cc	131.4	20.1	28.9	117.6	93.3	29.8	10.4	7.1	16.9	50.2	8.7	25.4	424.3	201.9	19.6	59.9	102.8
GOT20	cc	48.9	16.2	29.0	104.1	84.0	14.3	4.4	6.1	11.3	44.9	5.3	19.1	196.1	162.9	16.4	52.9	85.2
GOT5cc	ultra-cc	128.2	18.3	37.2	161.9	121.3	19.2	4.5	8.3	14.4	76.5	4.7	24.6	342.3	240.9	21.9	72.8	124.9
GOT26	ultra-cc	123.6	28.6	43.6	205.5	150.6	23.0	9.6	9.7	20.1	88.9	5.6	28.6	307.7	303.4	26.6	85.2	142.3
GOT23	zeo vein	0.1	0.1	3.3	7.1	11.7	4.6	0.1	2.3	4.1	5.7	2.7	6.1	10.8	48.6	2.8	8.6	15.9
GOT5v	zeo vein	16.1	0.1	9.5	27.2	27.4	5.0	3.1	3.4	4.9	13.4	3.3	11.1	23.7	81.6	6.1	17.3	29.6
GOT12	cal vein	54.8	0.1	5.0	140.6	20.5	7.3	0.1	3.6	5.0	22.3	3.3	46.7	28.8	1333.2	10.0	21.7	26.1
IBOhwhost	HW host	119.8	62.6	44.5	86.6	126.1	27.5	21.7	19.7	38.1	52.7	4.8	33.2	301.2	487.4	47.9	124.7	266.7
IBOfwhost	FW host	184.0	55.8	48.1	56.9	147.5	27.4	17.5	21.0	31.0	50.5	12.5	25.8	347.2	487.8	33.3	107.2	212.5
IBO1-4	breccia	128.3	46.4	46.7	42.8	124.4	17.8	14.7	16.7	24.2	43.9	10.0	24.3	198.1	380.8	25.2	79.6	163.9
IBO1-3	proto-cc	162.6	57.5	49.4	82.6	228.1	25.7	17.9	20.2	30.2	49.9	12.0	26.6	322.1	468.9	33.7	101.4	205.1
IBO1-1	cc	62.8	17.6	21.5	23.1	95.9	13.9	7.7	7.3	8.3	34.1	32.4	29.6	205.1	139.6	14.3	38.2	75.4
IBO1-5	gouge	171.0	54.1	47.5	58.3	168.2	25.5	18.0	20.0	31.0	45.0	11.7	27.4	324.8	445.1	34.0	97.1	201.2
SEL2	host	190.2	37.2	38.9	64.5	192.4	19.7	12.7	13.4	22.1	70.0	5.2	26.4	477.6	345.2	27.7	94.2	181.3
SEL3	DZ cc	33.5	33.0	32.2	60.7	198.0	38.8	8.8	12.8	22.8	45.8	3.0	24.8	346.3	330.6	28.7	81.0	171.1
SEL1	ultra-cc	65.6	21.7	34.5	176.0	141.1	27.5	6.1	9.5	14.1	74.9	8.9	29.7	129.1	267.8	24.3	94.6	118.1
RSD / %		2.6	8.2	3.5	1.1	1.6	2.7	12.3	1.6	6.3	1.3	2.2	3.1	0.2	0.5	1.4	1.0	1.3

Table S3. Absolute (ASD) and relative standard deviation (RSD) for major element analysis in XRF determined on Whin Sill dolerite (Govindaraju, 1994). Concentrations in weight percent.

	SiO_2	TiO_2	Al_2O_3	Fe_2O_3	MnO	MgO	CaO	Na_2O	K_2O	P_2O_5	SO_3	Total
Reference value	***51.31***	***2.54***	***14.04***	***13.51***	***0.18***	***5.31***	***8.87***	***3.10***	***1.36***	***0.30***	***0.00***	
27/04/2017	51.37	2.51	13.70	13.56	0.17	5.35	8.74	2.79	1.31	0.30	0.06	99.89
17/05/2017	51.64	2.52	13.80	13.56	0.17	5.36	8.74	2.77	1.31	0.30	0.07	100.24
30/05/2017	51.42	2.52	13.80	13.57	0.17	5.38	8.76	2.78	1.31	0.30	0.07	100.08
06/06/2017	51.49	2.51	13.80	13.59	0.17	5.35	8.75	2.78	1.32	0.30	0.07	100.12
28/06/2017	51.42	2.51	13.74	13.56	0.17	5.37	8.76	2.77	1.31	0.30	0.07	99.98
06/07/2017	51.36	2.51	13.74	13.56	0.17	5.34	8.76	2.79	1.31	0.30	0.07	99.91
25/09/2017	51.69	2.53	13.96	13.56	0.17	5.35	8.82	2.81	1.32	0.31	0.17	100.69
13/07/2017	51.57	2.53	13.98	13.58	0.17	5.41	8.72	2.85	1.32	0.31	0.16	100.61
19/07/2017	51.66	2.52	13.91	13.57	0.17	5.37	8.79	2.82	1.32	0.31	0.16	100.60
01/08/2017	52.00	2.52	14.00	13.55	0.17	5.38	8.80	2.84	1.32	0.31	0.16	101.05
08/08/2017	51.53	2.52	13.98	13.46	0.17	5.36	8.79	2.82	1.32	0.31	0.17	100.42
09/08/2017	51.53	2.52	13.98	13.46	0.17	5.36	8.79	2.82	1.32	0.31	0.17	100.42
14/08/2017	51.89	2.52	13.94	13.55	0.17	5.38	8.78	2.84	1.33	0.31	0.16	100.86
08/10/2019	51.37	2.50	13.83	13.54	0.17	5.33	8.78	2.82	1.32	0.32	0.15	100.14
18/12/2019	51.50	2.50	13.77	13.53	0.17	5.32	8.79	2.90	1.33	0.32	0.14	100.27
12/02/2020	51.33	2.49	13.73	13.54	0.18	5.42	8.76	2.82	1.32	0.31	0.15	100.06
14/08/2020	52.17	2.51	14.27	13.45	0.17	5.26	8.77	2.86	1.32	0.32	0.15	101.26
ASD (wt.%)	***0.3***	***0.0***	***0.2***	***0.0***	***0.0***	***0.0***	***0.0***	***0.0***	***0.0***	***0.0***	***0.0***	
RSD (%)	***0.5***	***0.4***	***1.1***	***0.3***	***1.0***	***0.7***	***0.3***	***1.3***	***0.6***	***2.0***	***37.5***	

Table S4. Blank analysis of Li-tetraborate flux indicating the lower limits of detection (=average + 3ASD).

	SiO_2	TiO_2	Al_2O_3	Fe_2O_3	MnO	MgO	CaO	Na_2O	K_2O	P_2O_5	SO_3	Total
27/04/2017	0.05	0.00	0.16	0.02	0.00	0.10	0.02	0.10	0.00	0.00	0.01	0.47
17/05/2017	0.06	0.00	0.17	0.02	0.00	0.10	0.02	0.11	0.00	0.00	0.02	0.51
30/05/2017	0.06	0.00	0.16	0.02	0.00	0.10	0.02	0.11	0.00	0.00	0.01	0.51
06/06/2017	0.07	0.00	0.17	0.02	0.00	0.10	0.02	0.10	0.00	0.00	0.02	0.51
28/06/2017	0.06	0.00	0.16	0.02	0.00	0.10	0.02	0.11	0.00	0.00	0.02	0.51
06/07/2017	0.08	0.00	0.17	0.02	0.00	0.10	0.02	0.11	0.00	0.00	0.02	0.53
25/09/2017	0.27	0.01	0.25	0.02	0.00	0.12	0.04	0.14	0.00	0.01	0.05	0.91
13/07/2017	0.26	0.01	0.25	0.02	0.00	0.12	0.04	0.13	0.00	0.01	0.05	0.88
19/07/2017	0.22	0.01	0.23	0.02	0.00	0.12	0.03	0.13	0.00	0.01	0.04	0.80
01/08/2017	0.22	0.00	0.24	0.02	0.00	0.12	0.03	0.13	0.00	0.01	0.04	0.82
08/08/2017	0.22	0.01	0.24	0.02	0.00	0.12	0.03	0.13	0.00	0.01	0.04	0.82
09/08/2017	0.22	0.01	0.24	0.02	0.00	0.12	0.03	0.13	0.00	0.01	0.04	0.82
14/08/2017	0.23	0.01	0.23	0.02	0.00	0.12	0.03	0.13	0.00	0.01	0.04	0.82
08/10/2019	0.24	0.01	0.22	0.02	0.00	0.12	0.03	0.15	0.00	0.01	0.05	0.85
18/12/2019	0.00	0.00	0.04	0.02	0.00	0.08	0.02	0.14	0.01	0.03	0.07	0.41
12/02/2020	0.11	0.01	0.08	0.02	0.00	0.08	0.02	0.15	0.01	0.03	0.08	0.58
14/08/2020	0.02	0.01	0.05	0.02	0.00	0.08	0.02	0.15	0.01	0.03	0.08	0.47
Average	***0.13***	***0.01***	***0.17***	***0.02***	***0.00***	***0.10***	***0.03***	***0.13***	***0.00***	***0.01***	***0.04***	
ASD	***0.1***	***0.0***	***0.0***	***0.0***	***0.0***	***0.0***	***0.0***	***0.0***	***0.0***	***0.0***	***0.0***	
LLD	***0.400***	***0.010***	***0.283***	***0.024***	***0.003***	***0.133***	***0.049***	***0.168***	***0.008***	***0.016***	***0.084***	

Table S5. Relative standard deviation (RSD) for trace element analysis in XRF determined on BHVO-1, BIR-1, and BCR-1 basalts (Imai et al., 1995). Concentrations in parts per million.

	Ba	Ce	Co	Cr	Cu	Ga	La	Nb	Nd	Ni	Rb	Sc	Sr	V	Y	Zn	Zr
BHVO-1	***134.4***	***38.1***	***44.9***	***287.6***	***137.2***	***21.3***	***15.4***	***18.5***	***24.8***	***120.0***	***9.5***	***31.4***	***399.2***	***313.8***	***26.2***	***105.1***	***174.6***
Feb-19	133.7	37.0	45.9	284.0	162.5	21.7	13.4	19.5	23.0	125.9	10.1	29.1	396.1	307.3	27.3	123.5	181.0
Apr-19	141.0	37.1	45.0	282.9	158.9	21.7	14.1	19.6	24.2	126.9	10.3	29.6	396.6	309.9	26.9	121.8	180.7
Jun-19	137.2	37.8	43.7	285.7	160.3	21.4	12.2	19.5	23.5	126.3	10.2	30.2	397.0	310.2	27.2	121.9	181.3
Aug-19	145.3	42.4	46.2	282.5	157.8	22.5	17.3	19.6	25.3	127.4	10.6	30.6	395.9	308.4	26.9	124.1	179.1
Oct-19	132.8	41.6	44.2	285.3	158.1	22.3	15.4	19.4	24.7	126.8	10.4	30.9	396.8	310.1	27.2	122.3	179.4
Dec-19	142.2	36.9	45.5	284.8	155.4	21.3	14.9	19.4	24.5	127.6	10.5	30.6	395.6	308.7	27.1	123.2	179.4
Feb-20	141.5	40.0	46.1	283.6	157.4	22.2	13.9	19.6	22.8	124.1	10.7	28.8	397.1	310.9	28.2	122.7	179.7
Aug-20	139.9	37.4	45.5	281.6	167.0	20.0	12.8	19.6	23.0	127.5	10.2	29.5	397.2	310.0	27.7	123.7	181.6
RSD (%)	***3.1***	***5.7***	***2.0***	***0.5***	***2.3***	***3.7***	***11.3***	***0.4***	***3.9***	***0.9***	***2.1***	***2.6***	***0.2***	***0.4***	***1.6***	***0.7***	***0.5***
BIR-1	***6.8***	***1.9***	***52.2***	***392.9***	***120.7***	***15.5***	***0.6***	***0.6***	***2.4***	***168.9***	***0.2***	***43.2***	***108.6***	***320.6***	***15.6***	***70.4***	***14.8***
Feb-19	19.4	-0.5	50.1	382.9	129.2	16.0	2.2	2.9	1.3	171.2	2.7	39.8	108.6	321.9	16.7	69.9	15.8
Apr-19	20.2	-0.5	50.8	383.9	128.7	15.9	2.4	2.5	1.0	172.8	2.8	39.0	109.2	316.8	16.9	70.2	15.5
Jun-19	16.8	3.6	54.5	381.6	128.1	17.1	-0.7	2.4	3.7	171.1	2.4	40.5	109.5	320.4	17.2	68.8	15.6
Aug-19	19.5	-0.4	51.0	381.5	124.0	15.2	-1.5	2.6	2.5	174.4	2.5	38.3	109.4	319.1	16.6	68.2	14.5
Oct-19	17.1	-1.3	51.6	382.8	124.2	15.9	-2.1	2.9	1.3	173.7	2.6	40.4	109.6	320.3	16.9	69.7	14.5
Dec-19	17.2	5.8	53.0	385.6	124.2	15.5	-0.1	2.5	3.8	171.9	2.8	38.9	109.0	318.5	16.9	68.8	14.8
Feb-20	16.9	4.3	53.0	381.5	124.9	15.6	-1.1	2.4	1.8	171.7	2.9	39.6	109.0	318.7	17.5	69.5	14.4
Aug-20	19.5	1.5	50.4	386.1	133.2	16.0	-2.9	2.3	2.5	173.6	3.1	39.3	109.6	318.5	17.8	68.9	13.5
RSD (%)	***7.9***	***173.0***	***3.0***	***0.5***	***2.6***	***3.6***	***-416.0***	***8.3***	***48.2***	***0.7***	***8.4***	***1.9***	***0.3***	***0.5***	***2.5***	***1.0***	***5.2***
BCR-1	***683.3***	***53.9***	***37.6***	***13.5***	***19.6***	***22.2***	***25.5***	***12.7***	***28.7***	***11.7***	***46.6***	***32.4***	***334.9***	***404.4***	***36.9***	***128.5***	***190.3***
Feb-19	728.3	57.1	39.2	36.8	42.3	22.8	28.3	13.6	29.0	12.0	49.1	30.2	334.1	399.0	37.6	123.1	198.5
Apr-19	720.0	60.3	40.2	37.0	42.1	22.7	24.5	13.6	29.0	11.6	49.0	29.8	333.7	400.0	37.7	123.6	198.5
Jun-19	723.4	56.3	40.0	35.3	43.1	22.4	27.3	14.0	28.3	10.6	49.0	30.5	333.7	396.3	37.4	125.4	199.0
Aug-19	731.5	58.4	39.0	35.7	41.0	22.6	24.2	13.6	28.1	11.3	48.7	29.3	333.7	399.6	37.9	126.7	197.5
Oct-19	715.1	57.6	39.0	32.3	40.2	22.4	25.0	13.8	27.0	11.6	49.1	28.6	333.7	397.3	37.6	125.6	197.4
Dec-19	723.4	56.1	37.6	34.0	40.0	23.9	22.9	13.6	29.0	11.1	48.8	28.4	335.0	398.4	37.9	125.5	198.2
Feb-20	717.7	59.7	36.5	36.3	41.3	23.1	25.2	13.4	27.3	12.3	48.6	30.0	334.0	398.4	38.3	125.5	197.0
Aug-20	708.8	55.7	35.7	34.5	43.8	23.4	25.9	13.6	28.3	12.1	48.7	30.0	335.0	397.4	38.8	124.3	198.4
RSD (%)	***1.0***	***3.0***	***4.3***	***4.5***	***3.2***	***2.3***	***6.8***	***1.4***	***2.8***	***4.6***	***0.4***	***2.5***	***0.2***	***0.3***	***1.2***	***1.0***	***0.3***

Isocon Diagrams

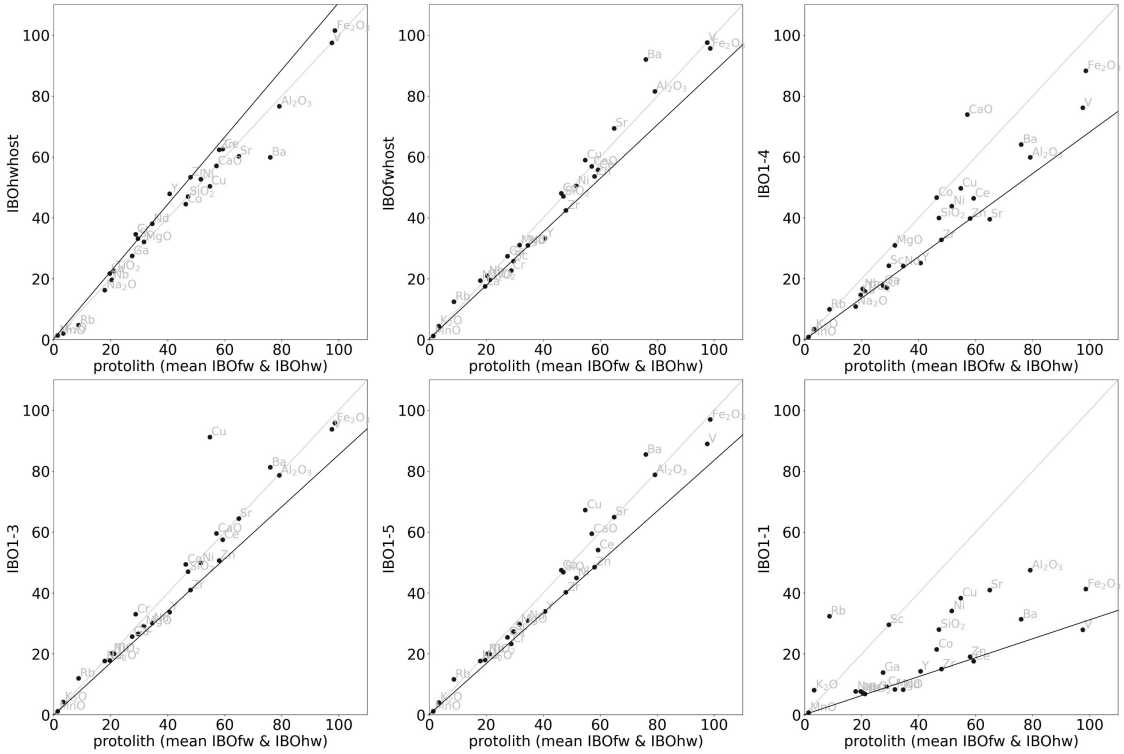

Figure S2. Isocon diagrams for Í Botni fault rocks. IBOhwhost & IBOfwhost – hanging wall and footwall host rock, IBO1-4 – breccia, IBO1-3 – protocataclasite, IBO1-5 – gouge, IBO1-1 – calcite-cemented fault vein.

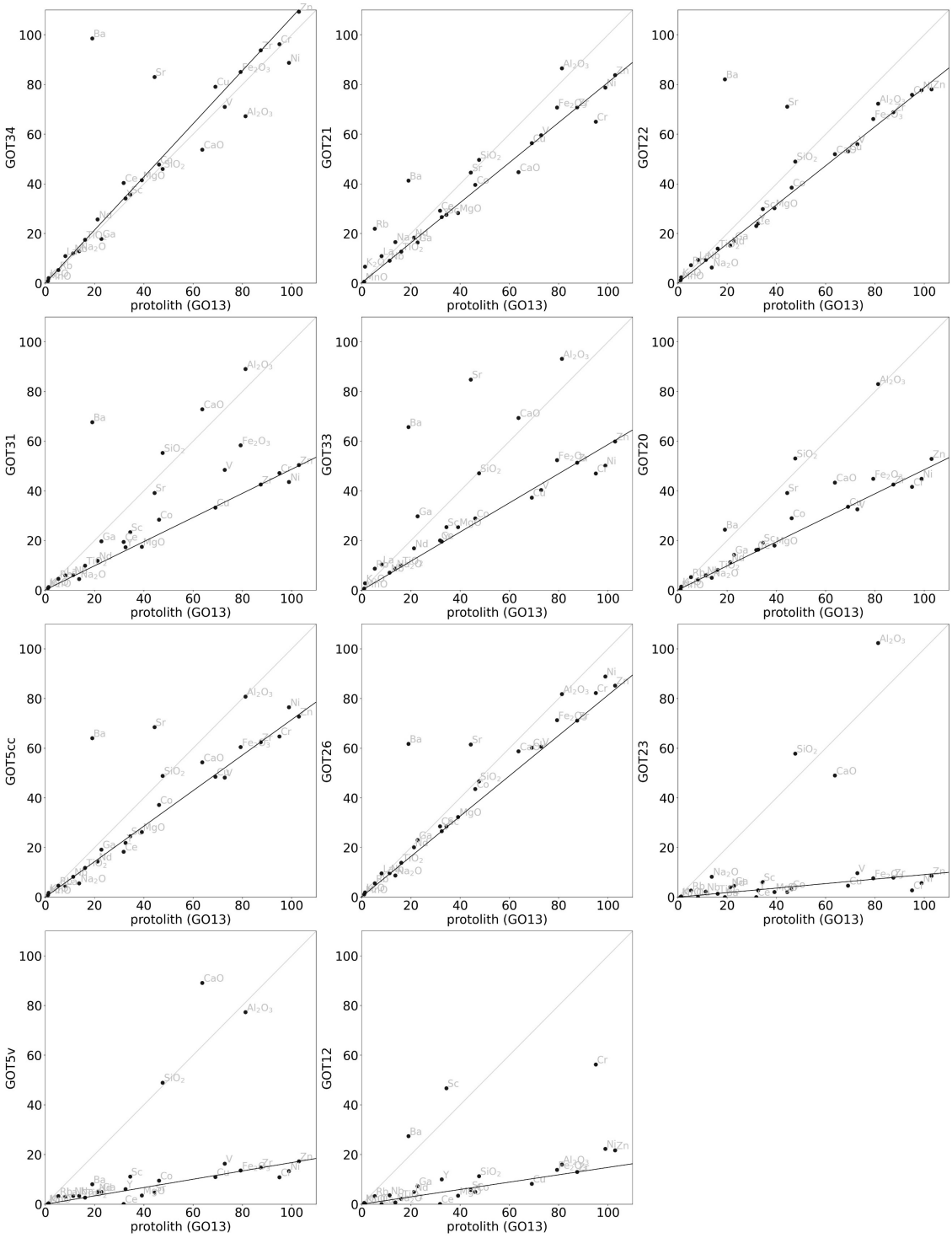

Figure S3. Isocon diagrams for the Gøtugjógv fault rocks. GOT34 – far damage zone, GOT21 – near damage zone, GOT22 – breccia, GOT31 – protocataclasite, GOT33 – cataclasite, GOT20 – cataclasite, GOT5cc – ultracataclasite, GOT26 – ultracataclasite, GOT23 – zeolite vein, GOT12 – calcite fault vein.

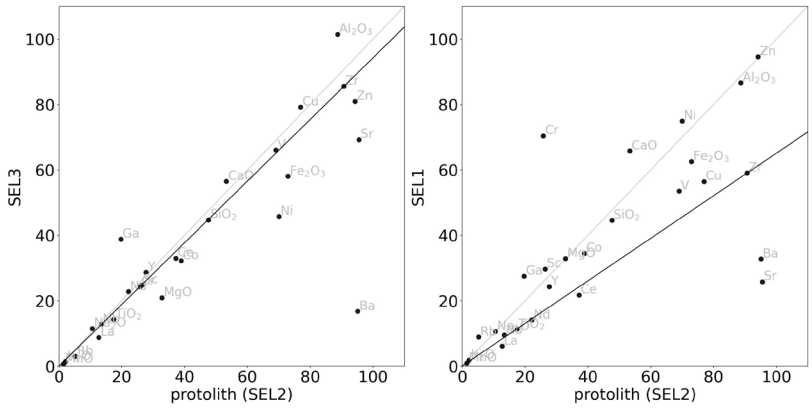

Figure S4. Isocon diagrams for the Selatrað fault rocks. SEL3 – breccia/cataclasite, SEL1 – ultracataclasite.

Mass Balance Estimation

Table S6. Mass balance calculation for the Gøtugjógv fault zone, estimating thickness of leached zone (in red, far ± near damage zone) required to provide amount of CaO, Al_2O_3, and SiO_2 gained by the fault core and the near damage zone, using Equation 3.3.

structure	sample	width	T_m			mass			
		meters	CaO	Al_2O_3	SiO_2	CaO	Al_2O_3	SiO_2	
far DZ	GO34		-0.212	-0.228	-0.098			leached	
near DZ	GO21	0.3	-0.132	0.315	0.288		0.09	0.09	
breccia	GO22	1.5	0.036	0.130	0.308	0.05	0.19	0.46	
proto-cc	GO31	0.1	0.399	1.098	1.288	0.04	0.11	0.13	
cataclasite	GO33	0.05	1.354	1.254	1.386	0.07	0.06	0.07	
cataclasite	GO5cc	0.3	0.194	0.393	0.439	0.06	0.12	0.13	
Ultra-cc	GO26	0.05	0.134	0.238	0.206	0.01	0.01	0.01	
zeolite vein	GO5v	0.05	7.276	4.625	5.080	0.36	0.23	0.25	
calcite vein	GO12	0.05	28.015	0.321	0.589	1.40	0.02	0.03	
						1.99	**0.84**	**1.17**	**added to core**
						-10.75 =mass/ (farDZ+0.5* nearDZ)/1.5	**-3.68** =mass/farDZ	**-11.97** =mass/farDZ	**m DZ leached**